Practical Design, Numerical Analysis, and Site Monitoring for Huge Arching Effect during Massive Excavation of Undercut Slope in Open-Pit Mine

Cheowchan Leelasukseree, *Assistant Professor, Chiang Mai University, Thailand; email:* cchan@eng.cmu.ac.th
Thirapong Pipatpongsa, *Associate Professor, Kyoto University, Japan; email:* pipatpongsa.thirapong.4s@kyoto-u.ac.jp
Apipat Chaiwan, *Senior Engineer, Mae Moh mine, Electricity Generating Authority of Thailand, Thailand; email:* apipat.c@egat.co.th
Noppadon Mungpayabal, *Senior Engineer, Mae Moh mine, Electricity Generating Authority of Thailand, Thailand; email*: noppadon.m@egat.co.th

ABSTRACT: *This paper reviews a successful case history where applications of numerical predictions for a massive excavation were undertaken for both Class A and Class B predictions. Forming a stable arch across the pit of an open-pit mine is beneficial to the design of an undercut slope. However, predicting the maximum stable undercut width under which the slope does not collapse is a challenging problem in geotechnical engineering. Slope undercutting techniques originally developed for 1g physical and centrifuge models were realized in practice for a full-scale design at the Mae Moh mine, one of the large coal open-pit mines in Southeast Asia, during the period of 2011 - 2017. Numerical analyses, along with in-situ measurements for data assimilation, were applied to test the novel design concept before and during the surface excavation. At the initial stage of excavating the undercut slope, the mine was studied in terms of forming an arch, by conducting a field experiment of a partial undercutting in Area 4.1, which was of monumental size, namely, 300 m in width and 80 m in height. It was planned that, during the first stage, from 2011 - 2014, Area 4.1 would be undercut 150 m and then back-filled using well-equipped surface and subsurface monitoring systems. After the completion of the first stage of the cut-and-fill, the undercutting and back-filling continued and the field experiment was successfully completed in 2017. A series of three-dimensional numerical models, using 3DEC, was generated and used in the preliminary studies. The numerical models favorably showed that the undercut slope was stable with large arching. The magnitudes of slope displacement from the numerical models and the field data were incomparable, but their directions and tendencies seemed to be quite well matched. Conclusively, the field monitoring data and the numerical model results of the undercut slope of Area 4.1 provided further understanding of undercut slope behavior. Therefore, the design of the undercutting method proposed in this study confirms that temporary cutting/excavating undertaken during construction can be done safely and economically.*

KEYWORDS: Slope Stability, Undercutting, Arching, Open-Pit Mines

**SITE LOCATION:** Geographic Database

INTRODUCTION

Although the percentage of fossil fuel consumption is decreasing due to emerging renewable energy resources, coal still remains the major source of energy in many regions of the world. Approximately one-fifth of the total electricity in Thailand is generated by mine-mounted power plants. Both the power plants and the adjacent open-pit mine are run by the Electricity Generating Authority of Thailand (EGAT). They are located in Mae Moh, Lampang, 630 km north of the capital (Figure 1). Thermal coal, amounting to 10 – 15 million tons, is taken from the 5 km-by-7 km open-pit mine and fed to the power plants annually (Mavong et al. 2013).

Approximately 200 million tons of minable thermal coal reserves currently remain in the Mae Moh basin of the Mae Moh mine. The Mae Moh basin is a typical syncline, namely, a trough of stratified rock layers. The two main layers, the top soil and the red bed, overlay the coal seams. The red bed consists of reddish stiff and highly fissured clay (Mavong et al. 2014; Mavong et al. 2013). Next, five coal seams, interbedded with gray claystone layers, lie under the red bed. The coal seams were named with letters as J, K, Q, R, and S. The overall thickness of the coal seams and gray claystone interburden are in the range of 300 m - 420 m. The underburden and base rock lie under Seam S. In addition, several thin clay seams unsystematically interbed in both the interburden and underburden layers. Moreover, a set of normal faults in the north – south direction is also found as a major geological structure in the basin.
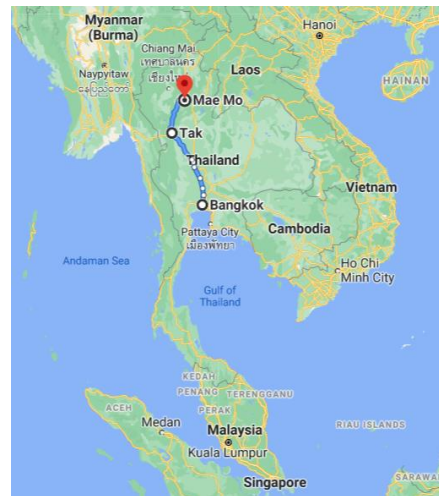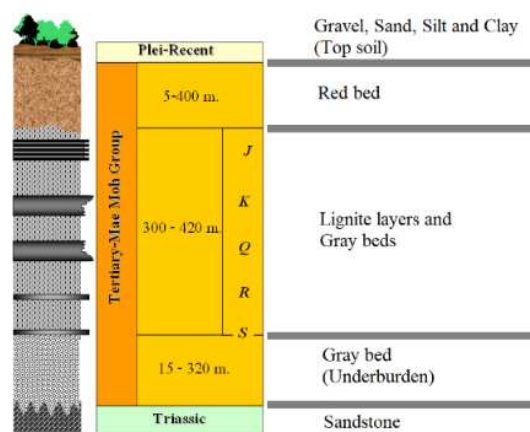

Figure 1. Location of Mae Moh.

In mining, undercutting is sometimes inevitable because of the orientations of the beddings and normal faults. For example, a cross-sectional plot of the northeast pit wall of the Mae Moh mine, called Area 4.1 and presented in Figure 2, shows the normal faults, beddings, and ground surface. The normal faults have cut the layers in Area 4.1 and have caused the formation of horsts and grabens. The pit wall stability of Area 4.1 is jeopardized when the coal seams below it are mined or undercut. The underburden blocks, placed on the low wall or footwall, have been displaced along the dip direction of the bedding. It is very likely that the blocks will slide along the very low friction angle plane, a thin clay seam called G1, and the gray claystone interface. The uppermost brown line in the figure represents the pre-mining topography of the ground surface. If the K and Q coal seams are excavated, as has been planned, the slope profile will be altered, as seen by the dashed blue line. G1's interface is daylighted on the slope for approximately 250 m. The shaded red block, reportedly 3 million cubic meters in size, will potentially turn into a massive sliding block. The very low friction angle of the interface is 12° – 14° (Mungpayabal 2005; Pipatpongsa et al. 2010). Slope failures associated with clay seams are also discussed in Ohta et al. (2010).

The full core photos taken from borehole NEI N29, where inclinometer I29 was installed (Khosravi et al. 2011), are shown in Figures 2(c) – (d). The material above the G1 interface is the underburden claystone rock mass, whose thickness is approximately 10 m. Its material properties are summarized in Table 1 for both the intact rock and the rock mass. The factor of safety is 0.61 from a simple calculation based on a 2D slope stability analysis using the interface friction angle (12°) and average dip angle of G1 (16°). The 2D slope stability analysis supports a conservative analysis because of the omission of the side resisting forces. Based on the 2D analysis, the undercutting of Area 4.1 would be unsafe and should be prohibited.

In 2011, a mine plan change was made for Area 4.1 of the Mae Moh mine, and the cut-and-fill mining method, based on arch action, was the substitute, as initiated by Pipatpongsa et al. (2009). Under arch action, the body force of the bulk materials is transferred from yielding zones to unyielding zones or from weaker parts to stiffer parts (Getzler et al. 1968; Guo and Zhou 2013; Iglesia et al. 2014; Ono and Yamada 1993; Terzaghi 1936). However, undercutting at the toe of a slope is conventionally considered to be a destabilizing mechanism in rock slope engineering (Hoek and Bray 1977), so it is not usual for the toe of a slope to be undercut. Therefore, it is of great importance to evaluate the maximum undercut width in the design concept for a practical technique. Theoretical models for undercut slopes have been studied by Pipatpongsa et al. (2013) and revised later (Pipatpongsa et al. 2016) to evaluate the factor of safety in the fully saturated condition with hydro-static water pressure on the bedding shear. The relationship between a stable width, and an inclined angle has been obtained

experimentally through a series of simple experiments using a block of compacted humid sand and varying its thickness, width, and length (Khosravi et al. 2016; Khosravi et al. 2009; Khosravi et al. 2011; Khosravi et al. 2012) in order to confirm the theoretical relations that develop. The results confirm that this novel procedure could be practically realizable for mining.

To apply the concept, the slope was partially undercut along the toe of the slope, following the results of physical models. As a result, the G1 interface was also partially daylighted. Then, backfilling was initiated to support the working face. The mining activities were alternated between undercutting and backfilling until the coal in Area 4.1 was totally mined and depleted. Although the G1 interface was partially daylighted, the potential sliding block above the interface remained questionable in terms of stability. Before changing the mine plan, numerical analyses were initially employed as a part of the studies conducted to understand the behavior of partially undercut pit wall stability (Leelasukseree et al. 2012; Ukritchon et al. 2018).
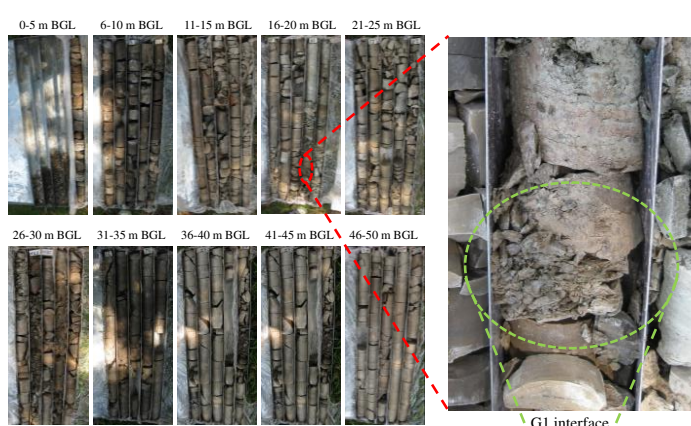

(a) Stratigraphy of Mae Moh basin
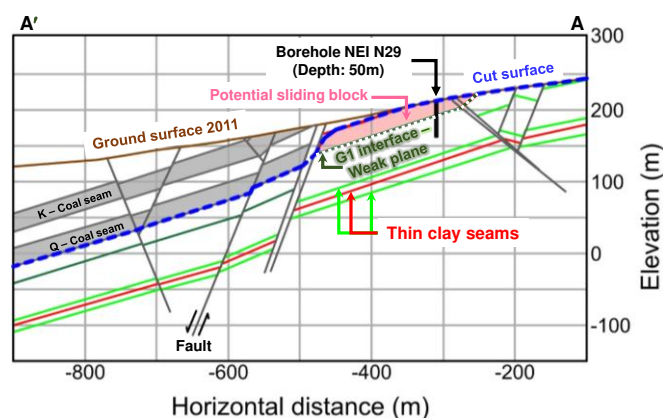
(b) Profile of Area 4.1 along A-A′ cross section
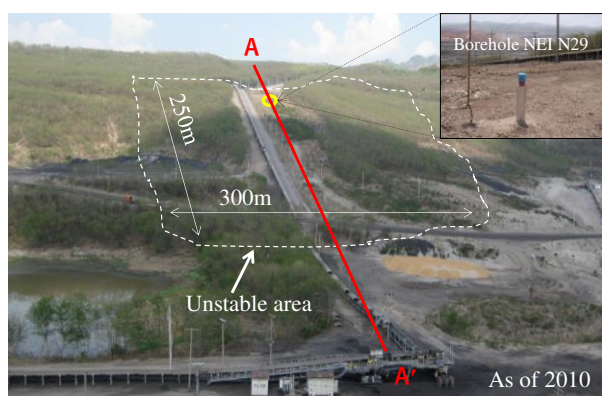
(c) Area 4.1 overview and location of borehole NEI N29

(d) Core photos of borehole NEI N29

Figure 2. General geological information of Mae Moh mine and Area 4.1.

PRELIMINARY STUDY USING NUMERICAL MODELING

To find the potential of the undercut mining in Area 4.1, mining engineers at the mine preliminarily studied a simple numerical model using 3DEC, a type of distinct element code (Itasca Consulting Group 2007). 3DEC was chosen due to resource availability. The engineers decided to use 3DEC among the many choices for the three-dimensional simulations. In the model, the slope dimensions—namely, the potentially sliding block thickness and the inclination of the G1 interface—were modeled to be the same as those expected in the field. The simple numerical model and its dimensions are illustrated in Figure 3. The slope was 900 m wide, 80 m high, 20 m thick, and had an inclination angle of 16°. Area 4.1's underburden claystone was placed on a huge table (shaded part). There were six undercuts, all equally 50 m in width, in the middle of the toe. The simple model consisted of 79,700 elements and 22,980 nodes for modeling the underburden claystone and the fixed platform.
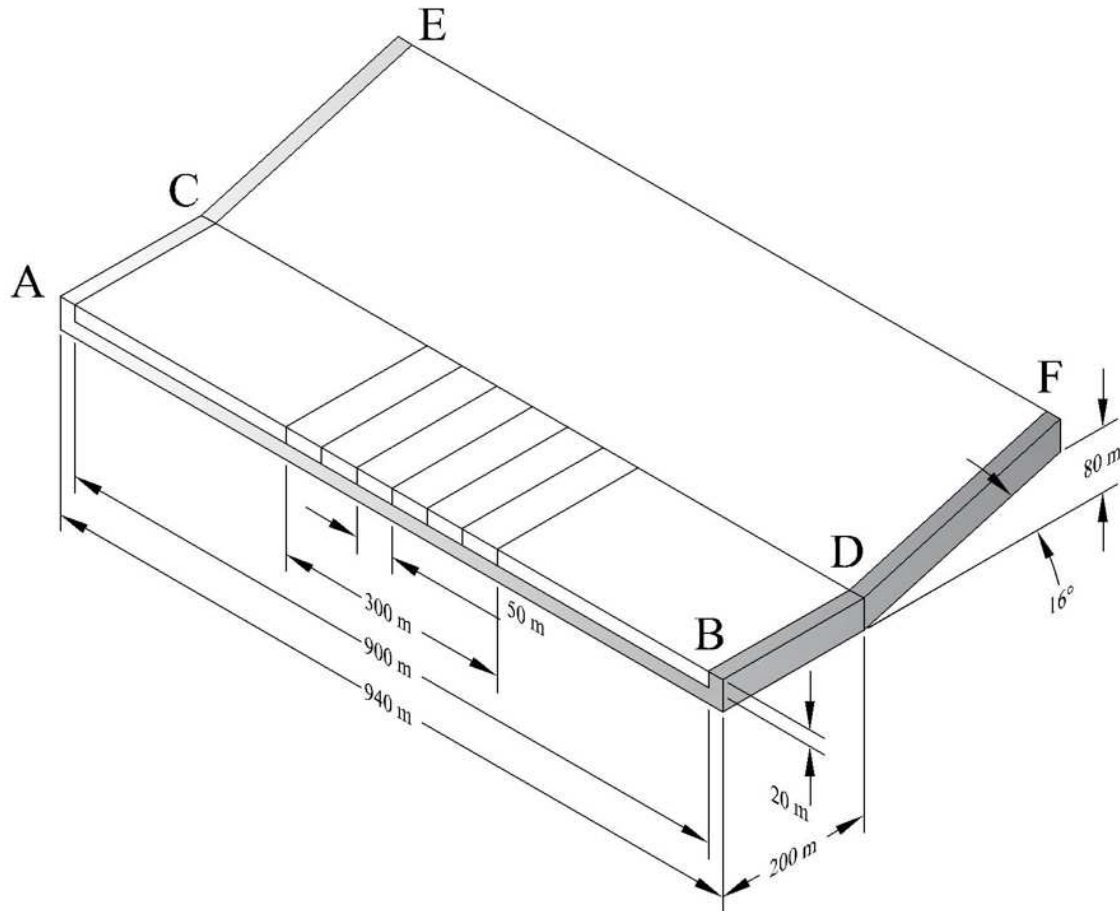
Figure 3. Simple numerical model of Area 4.1.

In this study, 3DEC, distinct element analysis software, was selected and used as aforementioned, although some available capabilities of 3DEC are similar to those of other types of commercial software, such as FLAC 3D reported by Khosravi et al. (2017), PLAXIS 3D reported by Ouch et al. (2016), PHASE 3D, etc. Each type of software, however, has different limitations and advantages, especially in terms of capabilities of integration and separation of the spatial domain. 3DEC became the appealing choice because of its exceptional deformation characteristics. 3DEC is capable of modeling and representing a system of blocks that would slip, separate, and rotate relative to one another without using interface elements. The blocks can also be assigned as rigid or deformable blocks. The structure-controlled failures are commonly expected and encountered in mining; therefore, 3DEC's features that allow for distinct element model separation and the modeling of the structure-controlled failures are impeccable.

It should be noted that the stress calculation in the blocks used in 3DEC is the forward-Euler integration scheme, or the incremental numerical algorithm. For each element in a block, the current state of stress at $t + \Delta t$, corresponding to the strain increment, is updated from the previous state of stress at time t.

The boundary conditions of the huge table and the rock mass were different. The table was wholly fixed, but the rock mass was only fixed at the toe end because it was not possible to computationally model the full extent of the slope. If there had been no fixed restraint at the toe end, the pillars would probably have been pushed by the action force from the sliding potential block after the slope was undercut.

The cohesionless contacts between the table and the rock mass were considered. The friction angle of 12° was assigned to the weak plane, the inclined contact (CDFE), to be as low as the friction angle of the G1 interface. For the other contacts (ACE, BDF, and ABDC), the friction angle of 21.4° was input and equaled the friction angle of the underburden claystone. The physical and mechanical properties of the rock mass will be presented later based on several laboratory tests.

Material Properties of Underburden Claystone Rock Mass

The material properties of the underburden claystone rock mass were inevitably required for the numerical modeling of the preliminary study of the Area 4.1 undercutting. As intact rocks are undisturbed rock samples that do not include planes of weakness or extents of fractures, but instead rock masses are cut into a number of blocks due to structural discontinuities, the material properties of the intact underburden claystone and the rock masses needed to be determined separately. According to the material test report (EGAT 1990), a total of 12 claystone core samples taken from two boreholes were classified into three claystone groups based on their colors and textures which were determined by the different geological formation processes that each group had undergone. The claystone core samples were subjected to the saturation stage, consolidation stage, and finally shearing stage under a fully drained condition for the triaxial testing.

Figure 4 shows the maximum and minimum effective compressive stresses at failure for each sample. Herein, the notation adopted in this study follows the sign convention used in soil mechanics, where compression is positive and tension is negative. It should be noted that one core sample was excluded because its appearance, texture, and test results deviated considerably from the others in the same sample set. The results of high pressure triaxial tests, conducted on three sets of core samples under effective confining pressures in the range of 1.1 – 15.1 MPa, are plotted in Figure 4. Subsequently, the high pressure triaxial test data were used to determine the material properties of the intact claystone and underburden claystone rock mass, e.g., the elastic constants and shear strength parameters.

The Young's moduli of all 11 samples of underburden claystone rock core were determined from slopes in the elastic range of the stress-strain curves obtained from the high pressure triaxial tests. Figure 5 shows the elastic modulus plotted against a variation in the effective confining pressure for each intact sample. The Young's moduli of all the samples were linearly fit and the elastic modulus of 1.1 GPa, determined at the zero effective confining pressure, was presumably the Young's modulus of the intact rock sample. The correlation coefficient (R) of the Young's modulus linear fitting was 0.330. Despite the intact rock and rock masses exhibiting pressure-dependent behavior, the Poisson's ratio of the intact rock sample can be determined from the linear relationship between the states of stress and strain in the elastic range of high pressure triaxial tests by assuming that Hooke's law is valid. However, only those obtained under the effective confining pressure of 1.1 – 6.1 MPa were in the acceptable range; therefore, the values ranging from 0.1 – 0.35 were obtained. Nevertheless, in many cases, the Poisson's ratio of the rock mass was larger than that of the intact rock sample, and the typical range of 0.25 – 0.40 was reported for the Poisson's ratio of the claystone (Gercek 2007). Consequently, the Poisson's ratio of the underburden claystone rock mass was assumed to be 0.3 for simplicity.
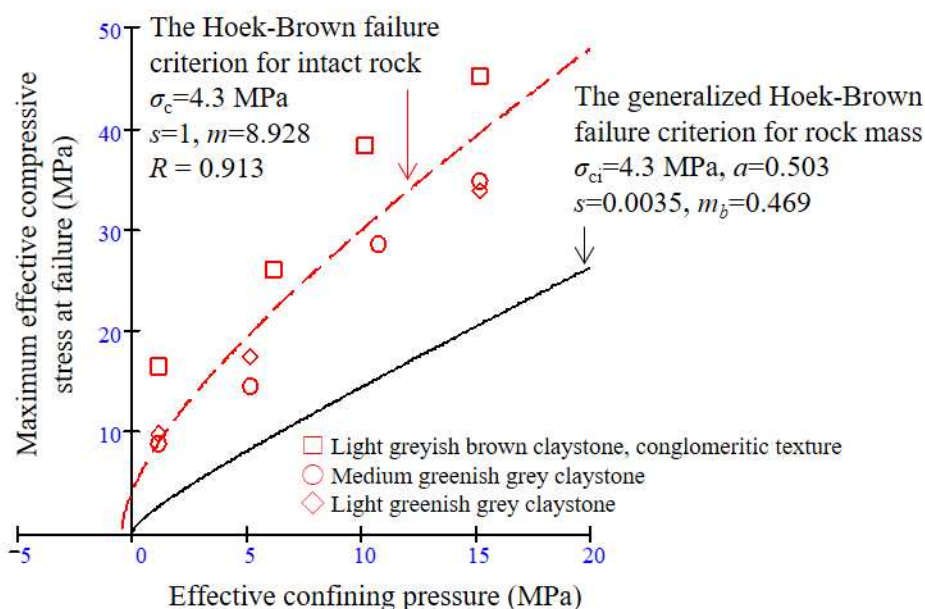

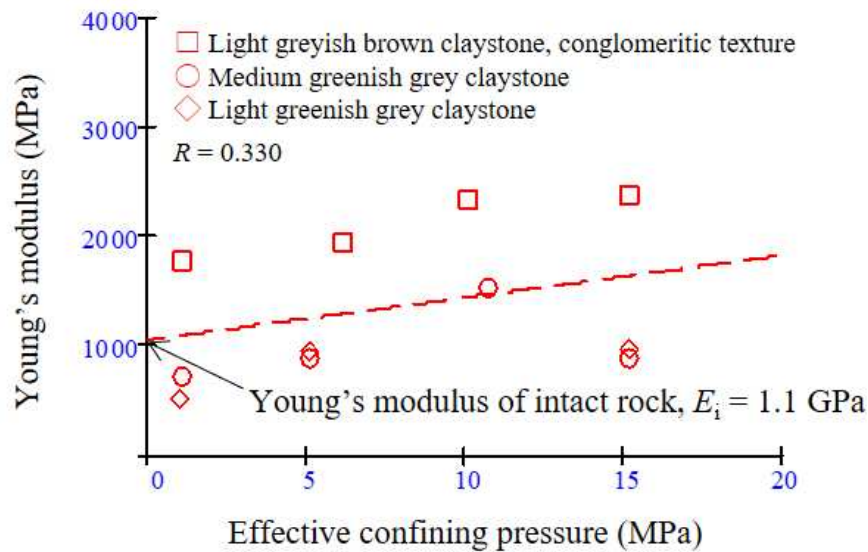*Figure 4. Principal stresses at failure for all samples.*

Figure 5. Elastic moduli and applied confining pressures.

Since actual rock masses exhibit heterogeneous, nonlinear, and anisotropic behaviours, the parameters of rock masses are downgraded from those of intact rocks by following the procedures described in the generalized Hoek-Brown failure criterion (Eberhardt 2012; Hoek 2007). To obtain the parameters of the underburden claystone rock mass for the generalized Hoek-Brown failure criterion, the states of the stresses at failure and the uniaxial compressive strength (UCS) of the intact rock samples were needed.

At first, the Hoek-Brown failure criterion of the intact underburden claystone was determined by fitting the maximum and minimum effective compressive stresses at failure from the high pressure triaxial tests and the UCS of the intact underburden claystone. The average and standard deviations in the UCS of the intact underburden claystone were reportedly 4.3 MPa and 2.7 MPa, respectively (EGAT 1985). Over 200 intact underburden claystone samples were tested for the UCS in the laboratory. After fitting 11 states of stresses at failure to the average UCS of the intact rock, the intact underburden claystone's Hoek-Brown failure criterion was able to be written as Eq. (1). The m constant was 8.928 and the s constant definitely equaled 1. The Hoek-Brown failure criterion of the intact underburden claystone is plotted in Figure 4 (red dashed line).

$$\sigma'_1 = \sigma'_3 + \sigma_c \left(m \frac{\sigma'_3}{\sigma_c} + s \right)^{\frac{1}{2}} \tag{1}$$

Next, the failure criterion of the underburden claystone rock mass was determined based on the generalized Hoek-Brown failure criterion proposed by Hoek et al. (2002) and Hoek and Diederichs (2006). The generalized Hoek-Brown failure criterion is expressed as Eq. (2).

$$\sigma'_1 = \sigma'_3 + \sigma_{ci} \left(m_b \frac{\sigma'_3}{\sigma_{ci}} + s \right)^{a} \tag{2}$$

This failure criterion requires six inputs: the UCS of the intact rock, the Geological Strength Index (*GSI*), m_i, the disturb factor, Young's modulus of the intact rock, and the expected minimum effective compressive stress. The UCS of the intact underburden claystone was 4.3 MPa, based on EGAT (1985), as stated earlier. The *GSI* of the underburden claystone rock mass was rated as "Blocky", based on site observations by engineers at the mine. A value of 4 was assigned to parameter m_i for the average value of the intact claystone. A value of 0.7 was given to the disturb factor because the mechanical excavation method was selected for mining in Area 4.1. The Young's modulus of the intact claystone, earlier estimated from the high pressure triaxial test results, was 1.1 GPa. The unit weight of the underburden claystone and the slope height were needed for

the expected minimum effective compressive stress in Area 4.1. The claystone density, the most familiar number for Mae Moh mine, was 1,950 kg/m^3. The height of the pit wall in Area 4.1 was 77 m (seven benches at 11 m per bench), as expected. From these inputs, the m_b, s and a constants of the generalized Hoek-Brown failure criterion were calculated. All inputs, the generalized Hoek-Brown criterion constants, and the estimated strength of the rock mass parameters are summarized and listed in Table 1.

Figure 6 also shows the states of stresses at failure of the intact claystone samples from the high pressure triaxial tests and Mohr-Coulomb failure criterion of the intact claystone and rock mass. The cohesion and friction angle of the intact claystone were linearly fit and calculated using the high pressure triaxial test data and Eq. (3). The cohesion and friction angle of the intact claystone were 3.457 MPa and 18.9°, respectively. The statistical measures for the linear and nonlinear regression of the triaxial test data were R=0.912 or R^2=0.833 and R=0.913 or R^2=0.834, respectively. For the underburden claystone rock mass, the friction angle was fit with the generalized Hoek-Brown failure criterion in the range of the expected minimum effective compressive stresses in Area 4.1. The friction angle of the underburden claystone rock mass was slightly higher than that of the intact claystone because the expected minimum effective compressive stress in Area 4.1 was as low as 0.94 MPa. Obviously, the strength of the underburden claystone rock mass was notably lower than the strength of the intact claystone, based on the generalized Hoek-Brown failure criterion (Figure 4) and the Mohr-Coulomb fit (Figure 6). Ultimately, the material properties required for the numerical analyses were the underburden claystone rock mass properties, which were reduced from the intact claystone properties. The Young's modulus, Poisson's ratio, and the cohesion and friction angle of the rock mass assigned to the numerical models were 0.2 GPa, 0.30, 0.138 MPa, and 21.4°, respectively.

$$\sigma_1' = \frac{2c'\cos\phi'}{1-\sin\phi'} + \frac{1+\sin\phi'}{1-\sin\phi'}\sigma_3' \qquad (3)$$

Table 1. Hoek-Brown classification, failure envelope range, and strength parameters of underburden claystone rock mass and interface.

|		
	Uniaxial compressive strength of intact rock, σ_{ci} (MPa)	4.3
	Geological Strength Index, *GSI* rated as "Blocky"	61
	Intact rock constant value, m_i "Claystone"	4
	Disturb factor, *D* "Mechanical excavation"	0.7
	Young's modulus of intact rock, E_i (GPa)	1.1
	Underburden claystone density (kg/m^3)	1,950
Failure envelope range	Slope height (m)	77
	Expected min. effective compressive stress (MPa)	0.94
Generalized Hoek-Brown criterion constants	m_b	0.469
	s	0.0035
	a	0.503
	Young's modulus of rock mass, E_m (GPa)	0.2
Rock mass strength parameters (Mohr-Coulomb fit)	Cohesion, c' (MPa)	0.138
	Friction angle, ϕ' (degree)	21.4
G1 interface strength parameters (Mungpayabal 2005)	Cohesion, c_i (MPa)	0
	Friction angle, ϕ_i (degree)	12
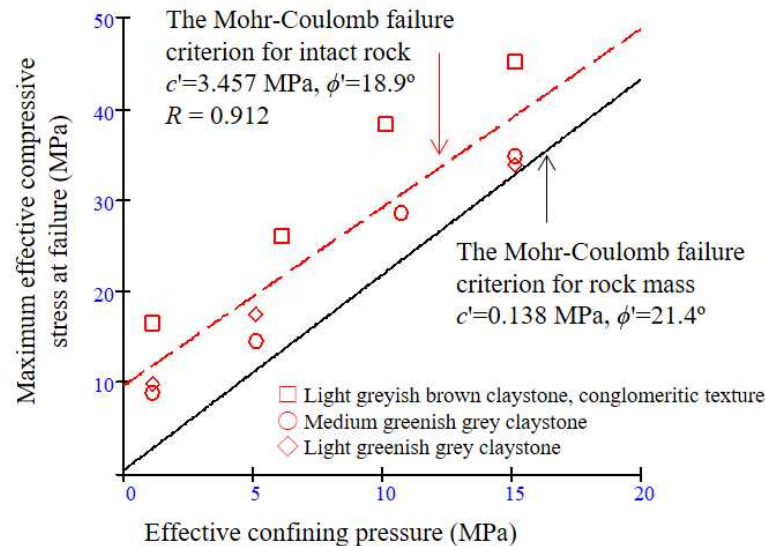
Figure 6. Mohr-Coulomb failure criteria of intact claystone and rock mass.

Sequential Excavation and Backfilling by Simple Numerical Model

After the completion of the model generation, boundary conditions, and rock mass property assignments, the sequential excavation of the model was analyzed. The sequential excavation comprised six steps. Steps 1 to 3 were only for undercutting 50-m-wide increments from left to right of the simple model. After Step 3, the total undercut width was 150 m. Steps 4 to 6 consisted of both undercutting and backfilling. The widths of the increments for undercutting and backfilling were also both 50 m in order to maintain the present undercut width or the daylight of the weak plane at 150 m. At Step 6, the widths of the undercutting and backfilling were as wide as 300 m and 150 m, respectively. The sequential excavation of the simple numerical model is graphically shown in Figure 7 with a 25-m grid spacing.

It should be noted that the backfill mostly consisted of underlying layers of limestone and overlying layers of compacted waste rock. Therefore, in this study, the strength parameters and unit weight of the backfill material were assumed to be the same as for the underburden claystone rock mass due to the lack of a laboratory investigation. As the backfill provides only a counterweight in the design, the failure of the backfill was not considered in the analysis.

Results of Simple Numerical Model

The results of the simple numerical model with the sequential excavation helped facilitate communication with the site engineers for the conceptual design. The total displacement and displacement vectors are presented in Figure 8, while the principal stress trajectories of the undercut slope are presented in Figure 9.

As the undercutting process was begun, the magnitude of the slope displacement above the undercutting area gradually increased as the excavation span continuously increased. The direction of the displacement vectors pointed to the excavation and was parallel to the dip vectors of the slope. Along the dip direction of the slope, the regions near the excavation showed larger magnitudes of displacement than the other regions near the slope crest. For the unmined regions, called pillars, the displacements on both sides of the excavation were relatively small. The maximum magnitude of the slope displacement occurring in Step 6, with the widest undercut span and backfilling, was 0.86 m. It was located above the undercutting face and near the edge of the backfill.

The axes of the principal stresses in the slope changed from their original condition, being reoriented by the influence of the undercutting. At the initial stage, the maximum compressive stress, σ_1, was aligned parallel to the dip vector of the slope, as shown in Figure 9(a). The magnitude of the maximum compressive stress progressively rose from the crest to the toe of the slope. The greatest magnitude of σ_1 was near the toe. On both side ends of the slope, the magnitude of σ_1 decreased because of side contact between the slope and the huge table or the boundary condition effects. When undercut, the σ_1 around the

excavation realigned in the tangential direction. The magnitude of σ_1 increased at the adjacently unmined toes. The changes in σ_1 in both direction and magnitude caused arching formation, or arching. The load along the centerline of the undercut span was tangentially transferred to both pillars. The arching then acted as a temporary support for a particular undercut span. As the undercutting continued, the span of the arch was broadened.
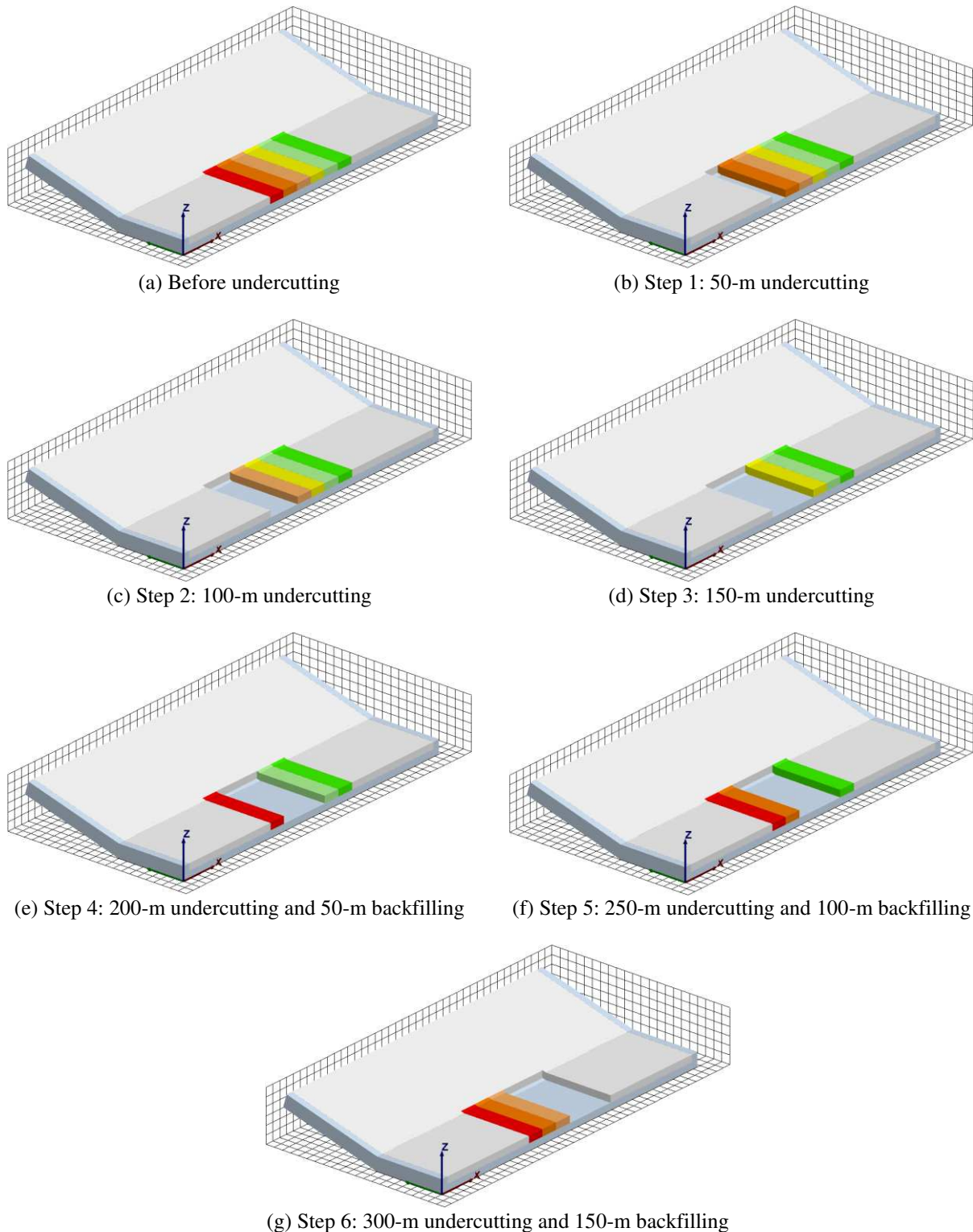

(a) Before undercutting   (b) Step 1: 50-m undercutting

(c) Step 2: 100-m undercutting   (d) Step 3: 150-m undercutting

(e) Step 4: 200-m undercutting and 50-m backfilling   (f) Step 5: 250-m undercutting and 100-m backfilling

(g) Step 6: 300-m undercutting and 150-m backfilling

Figure 7. Sequential excavation and backfilling.

(a) Step 1: 50-m undercutting

(b) Step 2: 100-m undercutting

(c) Step 3: 150-m undercutting

(d) Step 4: 200-m undercutting and 50-m backfilling

(e) Step 5: 250-m undercutting and 100-m backfilling

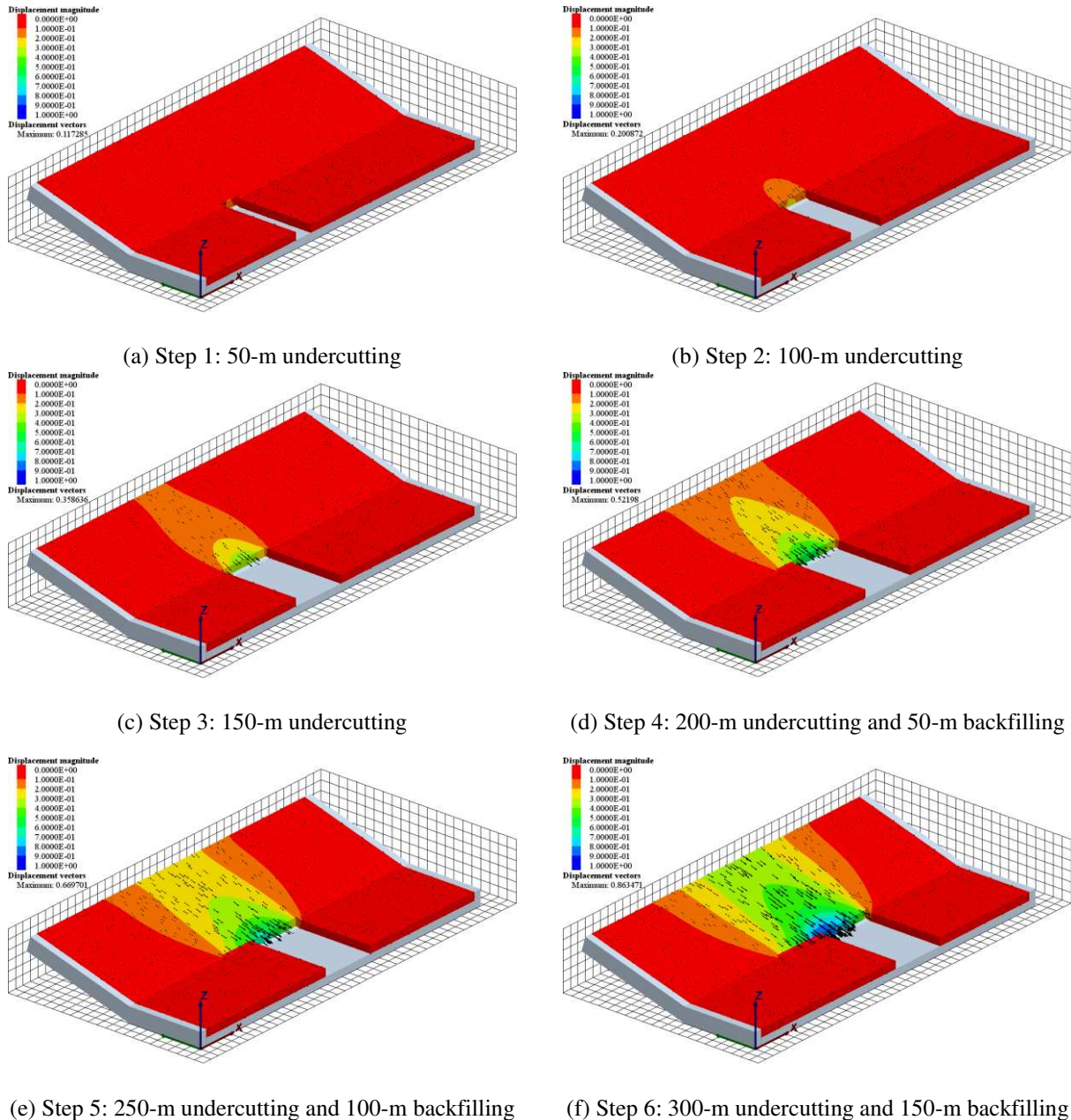(f) Step 6: 300-m undercutting and 150-m backfilling

Figure 8. Total displacement contour and vectors of simple Area 4.1 undercut slope model.

Steps 4 to 6 each consisted of a 50-m undercutting and a 50-m backfilling, as shown in Figures 9(e), 9(f), and 9(g). The G1 interface, or the weak plane, continued daylighting 150 m. The stiffness of the backfilling toes was less than that of the unmined toes; therefore, the arching was asymmetrical. The load was partially transferred to the backfill material. The stresses of the slope above the backfill increased slightly, but the increment in displacement decreased.

At each step of the sequential excavation, the factor of safety was calculated using the shear strength reduction technique (Matsui and San 1992). The factors of safety are presented in Figure 10 for comparison. The factors of safety for Steps 1 to 3 are seen to progressively decrease because of the undercut span extension. The factors of safety for Steps 4 and 5 are seen to slightly increase, but the factor of safety for Step 6 is seen to drop steeply to 1.00. This drop in the factor of safety for Step 6 stems from the accumulation of strain in the rock mass.
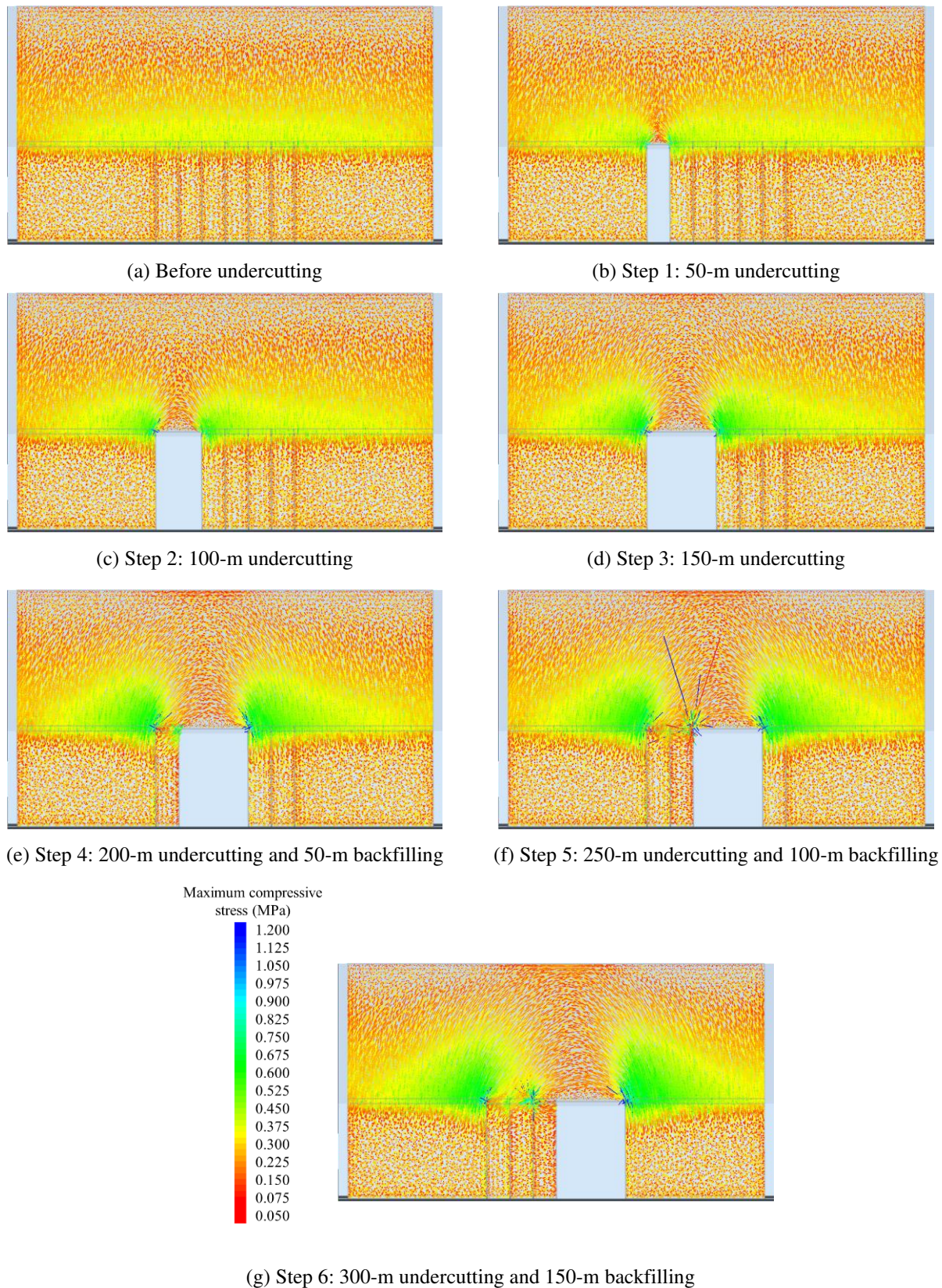
(a) Before undercutting

(b) Step 1: 50-m undercutting

(c) Step 2: 100-m undercutting

(d) Step 3: 150-m undercutting

(e) Step 4: 200-m undercutting and 50-m backfilling

(f) Step 5: 250-m undercutting and 100-m backfilling

Maximum compressive
stress (MPa)

| 1.200 |
| 1.125 |
| 1.050 |
| 0.975 |
| 0.900 |
| 0.825 |
| 0.750 |
| 0.675 |
| 0.600 |
| 0.525 |
| 0.450 |
| 0.375 |
| 0.300 |
| 0.225 |
| 0.150 |
| 0.075 |
| 0.050 |

(g) Step 6: 300-m undercutting and 150-m backfilling

Figure 9. Principal stress trajectories and maximum compressive stress contours of simple Area 4.1 undercut slope model.
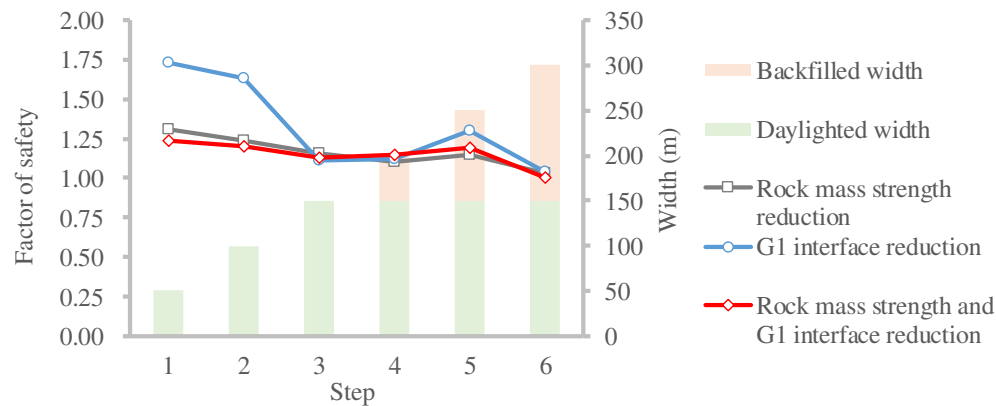
Figure 10. Factor of safety for each sequential excavation step using three reduction cases.

In this study, the built-in shear strength reduction technique, provided in 3DEC, was employed to determine the factor of safety. The shear strength parameters of the elements and/or contacts (geologic structures) are reduced by a shear strength reduction ratio and can be explained by Eq. (4). The factor of safety is determined by changing the shear strength reduction ratio iteratively until the equilibrium state of the model is obtained. The numerical procedure for searching for the factor of safety is based on the bracketing and bisection approach, as described in Dawson et al. (1999). Generally, the distinct element model is considered to be in the equilibrium state when the rate of change in kinetic energy reaches an insignificant amount. A damping factor is also needed in the law of motion. Instead of kinetic energy, 3DEC uses the force ratio (average unbalanced force to average applied force magnitude ratio for all nodes (grid points) in the model) as an indicator of the equilibrium state of the model. If the ratio is as low as the default threshold or limit at 1×10^{-5}, and the calculation iteration (or step) is less than 100,000 steps, the model state is considered to be in the equilibrium state.

$$\tau = \frac{c'}{FS} + \sigma' \tan\left(\frac{\tan^{-1} \phi'}{FS}\right)$$ (4)

For the simple model, the starting point or the initial configuration of the current step was updated after the completion of the numerical analysis of the previous step to determine the factor of safety using the method of strength reduction. Therefore, the factor of safety for each step depends largely on the history of the sequential excavation. The friction angle of 12° was assigned to the inclined contact or the weak plane, to be as low as the friction angle of the G1 interface, at the beginning of the model construction. The low friction angle of 12° was the residual friction angle of G1, the clay seam.

The simple models were run to obtain the factors of safety for two extra cases: namely, the claystone rock mass shear strength reduction and the G1 interface friction angle reduction. The calculated factors of safety are graphically shown in Figure 10. Overall, the rock mass strength primarily governs the undercut slope stability in most steps of the sequential excavation, except for Step 3 in which the factor of safety determined by the G1 interface reduction appears to significantly decrease. If the backfilled width does not take place, the undercut slope will not be stable. Comparatively, the factors of safety determined by the simultaneous reduction in the rock mass strength and the G1 interface seem to be on the safe side for practical design because the minimum value was achieved when the factors of safety approached one at the maximum accumulated undercut width.

Figure 10 shows the variation in factors of safety of the simple model under three cases, which were the rock mass strength reduction, the G1 interface friction angle reduction, and both the rock mass strength and the G1 interface friction angle reduction. The total height of the stacked bar graphs of the backfilled width and the daylighted width represent the accumulation of the undercut width at the G1 interface level.

The G1 interface progressively destabilized the undercut slope in Steps 1 – 2 and 2 – 3, due to a considerable decrease in the factor of safety. The gradient of the factor of safety for the G1 interface friction reduction shows a substantial sensitivity with the sequential excavation step; therefore, the stability of the undercut slope is rather governed by the G1 interface before backfilling. However, after backfilling in Steps 4 – 6, the rock mass strength governs the undercut slope stability again. Thus,

the rock mass strength becomes the key to governing the undercut slope stability when backfilling is applied. Due to the accumulation of the undercut width, the factors of safety in all reduction cases converge to 1.0 in Step 6, at which the rock mass and the G1 interface failed simultaneously.

Hence, the factor of safety calculated in Figure 10 was governed by either the claystone rock mass or the G1 interface, depending on the sequential excavation step. In the simple model, the stability of the undercut slope was marginal when the accumulation of the undercut width and the backfill were 300 m and 150 m, respectively, for which the factor of safety equaled 1. Therefore, the base sliding surface and lateral resistance or deep-seated failure would occur simultaneously at the final step. Consequently, no strength reduction was applied to the G1 interface (interface friction angle of 12°) or the claystone rock mass (friction angle of 21.4° and cohesion 0.138 MPa). Based on the simple numerical analyses, the engineers and mine administration decided to undercut and mine the coal in Area 4.1. Area 4.1 became a large-scale experiment for undercutting in a weak rock mass (Mavong et al. 2014). The designs and plans for Area 4.1 of the mine were initiated in 2010.

AREA 4.1 MINE PLAN AND SLOPE MONITORING SYSTEM

The mine plan for Area 4.1 was practically designed and divided into two operational stages: the 1st Stage and the 2nd Stage. Due to working space constraints, the G1 interface was expectedly daylighted, approximately 100 m and 140 m at the end of the 1st and 2nd Stages, respectively. The 1st and 2nd Stages' mining periods were from the middle of 2011 to the middle of 2014 and from 2014 to 2017, respectively.

Mine Plan

The mining sequence for the 1st Stage in Area 4.1 was planned as presented in Figure 11. The development and mining sequences began by cutting a main access ramp. To lower the potential block mass and driving force, highly laminated claystone layers, referred to as the "Marker bed", were mined from an elevation of 192-236 msl (Figure 11(a)). Then, the cut-and-fill mining method was employed to obtain the coal. Area 4.1 was mined and backfilled from an elevation of 126-192 msl (Figures 11(a) to (c)).
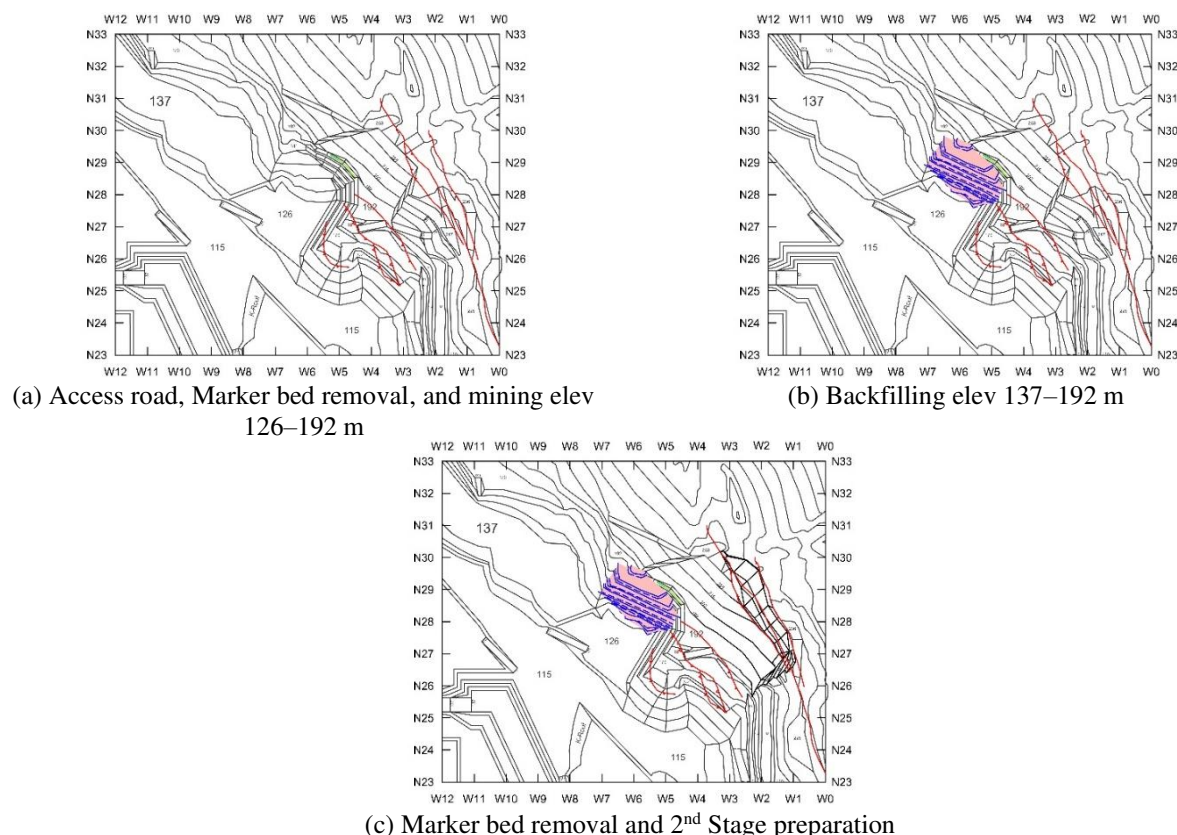

(a) Access road, Marker bed removal, and mining elev
126–192 m

(b) Backfilling elev 137–192 m

(c) Marker bed removal and 2nd Stage preparation

Figure 11. Sequential excavation of the 1st Stage in Area 4.1.

The undercutting in Area 4.1 was periodically photographed for archival purposes; some of the photographs are presented in Figure 12. The mine equipment was moved to Area 4.1 and the site preparation began in April 2011. Three months later, in July 2011, the Marker bed was ready to be excavated; by August 2011, it had been totally removed. The undercutting of the northern part of Area 4.1 began in August and reached an elevation of 170 msl by January 2012. The undercut span was approximately 80 m. The undercutting continued and reached an elevation of 137 msl by April 2012. The undercut width was approximately 90 m. Between May and June 2012, the backfill, comprising 30,000 cubic meters, was placed from an elevation of 115-192 msl. The undercut width was then shortened to 30 m. The undercutting was restarted and continued in the southern direction in August 2012. The 1st Stage was completed in May 2014. Finally, the undercut width had been extended to approximately 100 m by the end of the 1st Stage.

(a) Access road and Marker bed removal in 1st Stage (as of August 2011)


(b) Mining elev 170 m in 1st Stage (as of January 2012)

(c) Marker bed removal and 2nd Stage preparation in 1st Stage (as of April 2014)

Figure 12. Photographs of the 1st Stage in Area 4.1.

The mining sequence of the 2nd Stage is depicted in Figures 13(a) to 13(c). In Figure 13, the daylighted G1 interface and the normal faults in Area 4.1 are represented by green and red lines, respectively. The 2nd Stage was launched by mining the interburden and coal from an elevation of 104-192 msl during the period of 2014 to 2016. At the beginning of 2017, the backfilling of the 2nd Stage began and was completed in October 2017. The undercut face could not be fully backfilled and supported, as presented in Figure 13(c), because of the working space constraints. Consequently, the G1 interface (green line) was still daylighted on the undercut slope face for a length of 190 m.
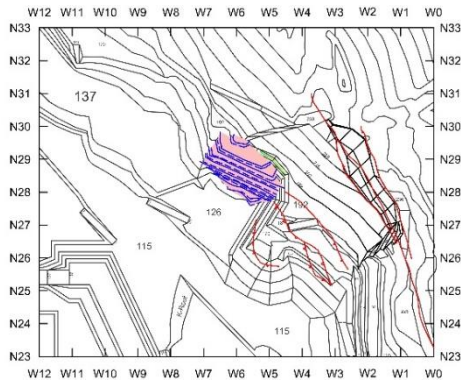
(a) At the beginning of 2nd Stage
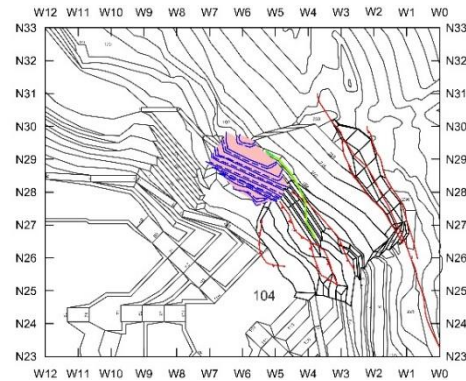
(b) Mining elev 192–104 m
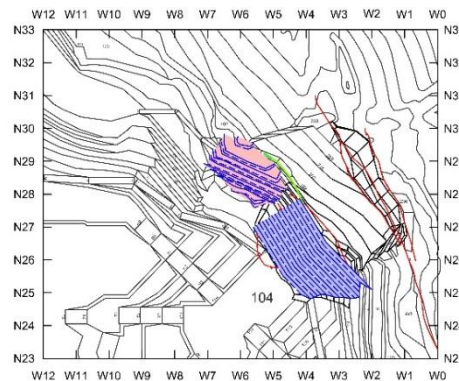
(c) Backfilling elev 104–192 m

(d) Aerial view at end of 2nd Stage (as of October 2017)

Figure 13. Sequential excavation of the 2nd Stage in Area 4.1.

Slope Monitoring System

Concurrently with the mining activities in Area 4.1, a slope monitoring system was set up. The groundwater pressure in the G1 interface was monitored and recorded by four vibrating wire piezometers, the surface and subsurface displacements were monitored and digitally recorded by three inclinometers, and the surface displacements were also monitored and recorded by the Robotic Total Station consisting of 48 prisms.

To condense the surface displacement monitoring data, the data from only 13 of the 48 prisms during undercutting are presented in this paper. In Figure 14, it is seen that these prisms were placed in three areas: the Upper Floor, Mid Floor, and Lower Floor. The Upper Floor, Mid Floor, and Lower Floor were at elevations of 236 msl, 203 msl, and 192 msl, respectively. Five prisms, SD05, SD06, SD09, SD11, and SD12, were installed in the Upper Floor, the uppermost part of Area 4.1. Another five prisms, SD13, SD14, SD15, SD16, and SD17, were installed in the Mid Floor. The last three prisms, SD19, SD20, and SD38, were placed in the Lower Floor, near the undercut slope face.

Three inclinometers, I192, I203, and I29, were also installed in Area 4.1 between February and March 2012 at elevations of 192, 203, and 232 msl, respectively. They were employed to monitor both the surface and subsurface displacements during the undercutting. The locations of the inclinometers are represented by yellow circles in Figure 14. I192 was placed above the pillar, outside the undercut face. I203 was installed in the upper surface of the undercut slope during the 1st Stage. I29 was also installed in the upper surface away from the undercut face and next to the Upper Floor prisms. All the inclinometer borehole lengths were approximately 40 m below the ground surface and through the G1 interface.
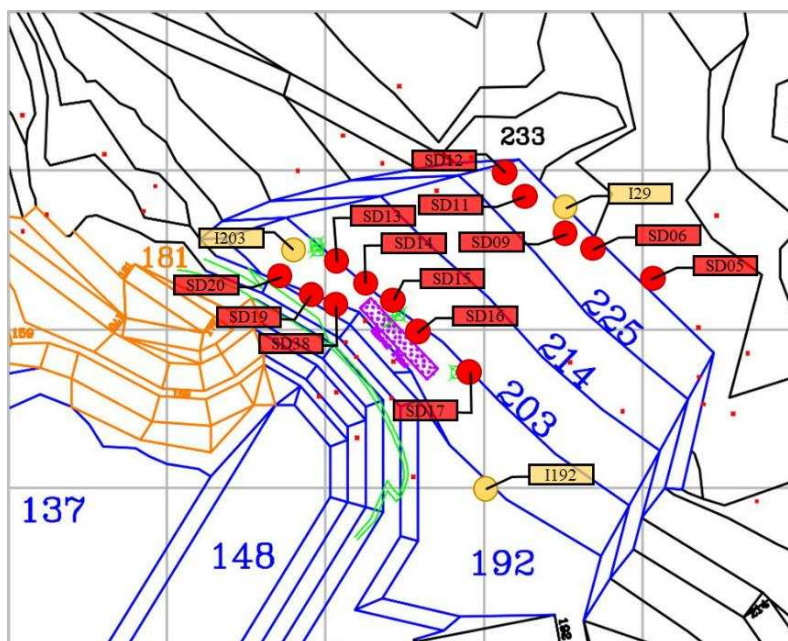

Figure 14. Locations of prisms and inclinometers in Area 4.1.

After the mine plan for Area 4.1 had been completed and approved by the mine administration, a series of numerical analyses was established. Its focus was the end of the 1st and 2nd Stages. The numerical analyses were simultaneously performed during the mine development in Area 4.1.

Undercut Slope Monitoring Data – Inclinometers

In the 1st Stage, measurements of the small surface and subsurface displacements were taken by I192 and I29 due to their locations. I192 and I29 were installed above the pillar and the uppermost part of the undercut slope, respectively.

Measurements of the substantial surface and subsurface displacements were taken by I203. The data measured by I203 are plotted in Figure 15. Large displacements of the orthogonal axes of the inclinometer (A and B axes) were measured and

recorded from the ground surface to a depth of 12 m. The depth of 12 m was indicated as the depth of the G1 interface. Along with the progress of the mining activity and the rainy season, the slope was slowly displaced and borehole I203 was gradually bent and totally sheared off by September 2012. The maximum surface and subsurface displacements at the G1 interface were 0.097 m and 0.088 m, respectively. The displacements measured by I203 were likely to be in the G1 interface dip direction. The data obtained by I203 revealed that the ground surface of the potential sliding block above the G1 interface was slightly more displaced than the subsurface.
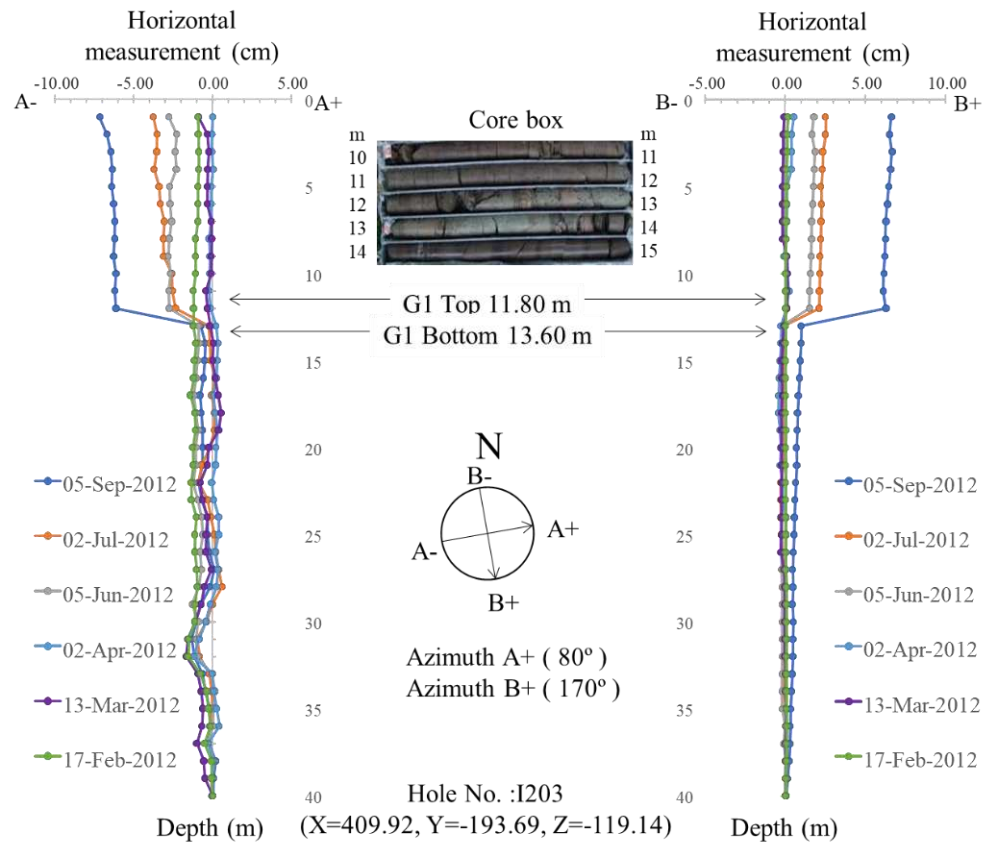

Figure 15. Surface and subsurface displacements measured by I203.

Undercut Slope Monitoring Data - Robotic Total Station with Prisms

The monitoring data for the ground surface displacements during the undercutting of Area 4.1 from 13 prisms are presented in Figure 16 along with the amounts of precipitation. The scheduled preventive maintenance program and an accidental system failure caused the monitoring to be discontinued. However, the monitoring data that were collected were still valuable. In Figure 16, the monitoring data are colorized according to the installation locations of the prisms. The ground surface displacement monitoring data on the Upper Floor, Mid Floor, and Lower floor have been colorized in yellow, green, and purple, respectively.

The surface displacements of the Upper, Mid, and Lower Floors – presented as the changes in the measured distance between the total station and the monitored prisms – were approximately -0.10 m, -0.25 m and -0.35 m, respectively, in early January 2013. The negative values indicate that the prisms displaced toward the total station. It is clear from the figure that the Lower Floor had the largest displacement because of its vicinity to the undercut face, while the Upper Floor had the smallest displacement. It should be noted that the surface displacement, measured by the Robotic Total Station with prisms (Figure 16), is a result of the interface shearing as captured by inclinometer I203 (Figure 15) and the deformation of the potential sliding block.
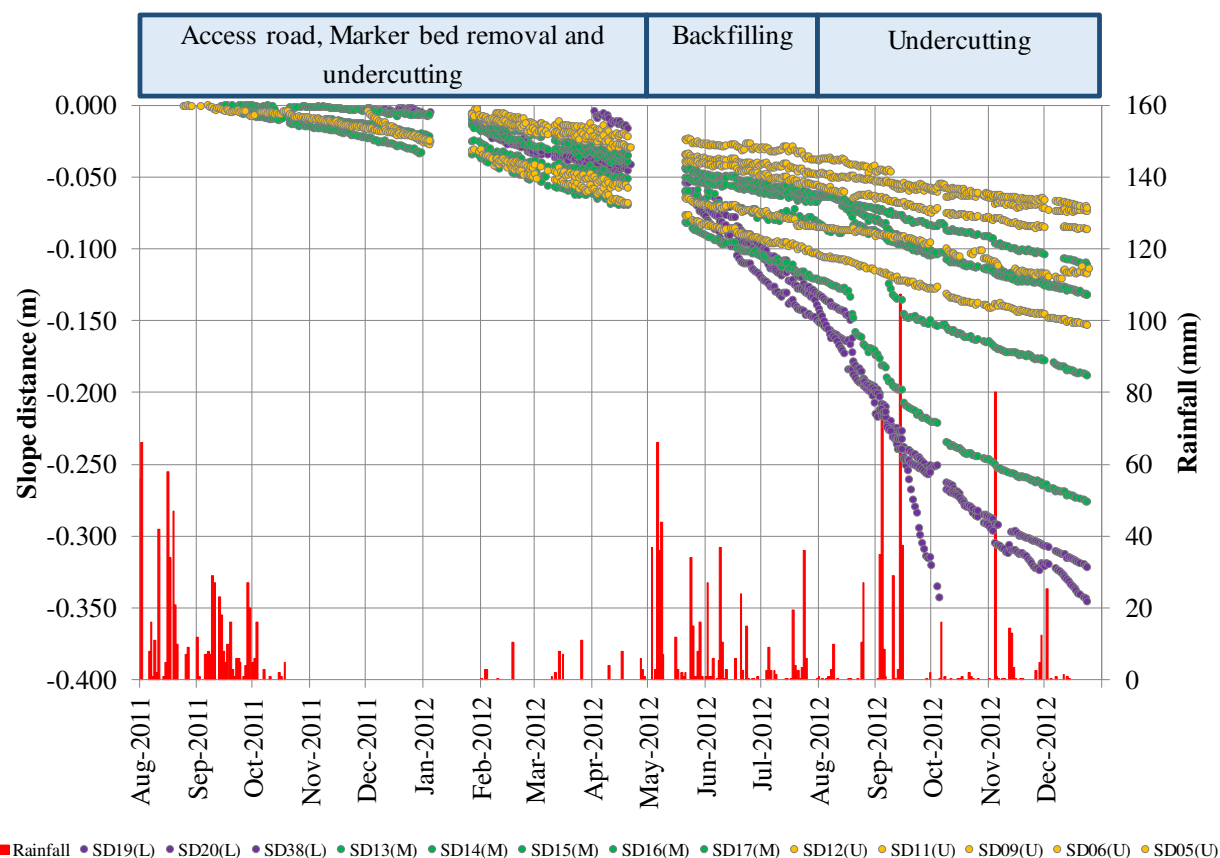
Figure 16. Surface displacements measured by prisms and amounts of precipitation.

Unfortunately, the ground surface displacement monitoring data could only be presented for the period of August 2011 to early January 2013. The remaining data related to Area 4.1 were severely damaged and/or lost during the transfer of the mine data and the upgrade of the server. All possibly recoverable sources have been sought, such as old PCs and HDDs stored in the mine's warehouse. Some of the surface displacement monitoring data were able to be recovered. The additional monitoring data of the 2nd Stage will be presented later on.

NUMERICAL MODEL OF 1st STAGE OF AREA 4.1

To estimate the displacement magnitude and to understand the behavior of Area 4.1 after the undercutting, a numerical model of the 1st Stage was generated and analyzed for Class A predictions (analyses taken before the construction). In the field, the spacings of the bedding planes and the cross-bedding joints were very close, namely, in the range of 0.30 to 0.60 m, while two faults and one bedding interface were the only major geologic structures. The required number of blocks for the full slope kinematics (Boon et al. 2014) for Area 4.1 would be enormous and beyond the computational capability of a personal computer. Both topographic and geologic details were reduced and simplified to make the model generation feasible. Moreover, all the materials in the model were assumed as the underburden claystone rock mass.

The model started with a big rectangular block, as presented in Figure 17. The dimensions of the pre-mining ground surface were 700(W) × 600(L) × 320(H) m³ (Leelasukseree and Mavong 2012). The flat top surface of the block represented the original ground topography surface or pre-mining ground surface. The block was divided into mining and geologic structure surfaces. The mining surfaces consisted of the pre-undercut, the mine development (after the Marker bed was removed), and the end of the 1st Stage surfaces. The mining surfaces were used for simulating the sequential excavation. The geologic structure surfaces consisted of two faults and a weak plane (G1 interface). The sub-blocks in the model were able to slide along the geologic structure surfaces, which were the faults and the G1 interface. The 1st Stage model consisted of 579,461 elements and 460,827 nodes.
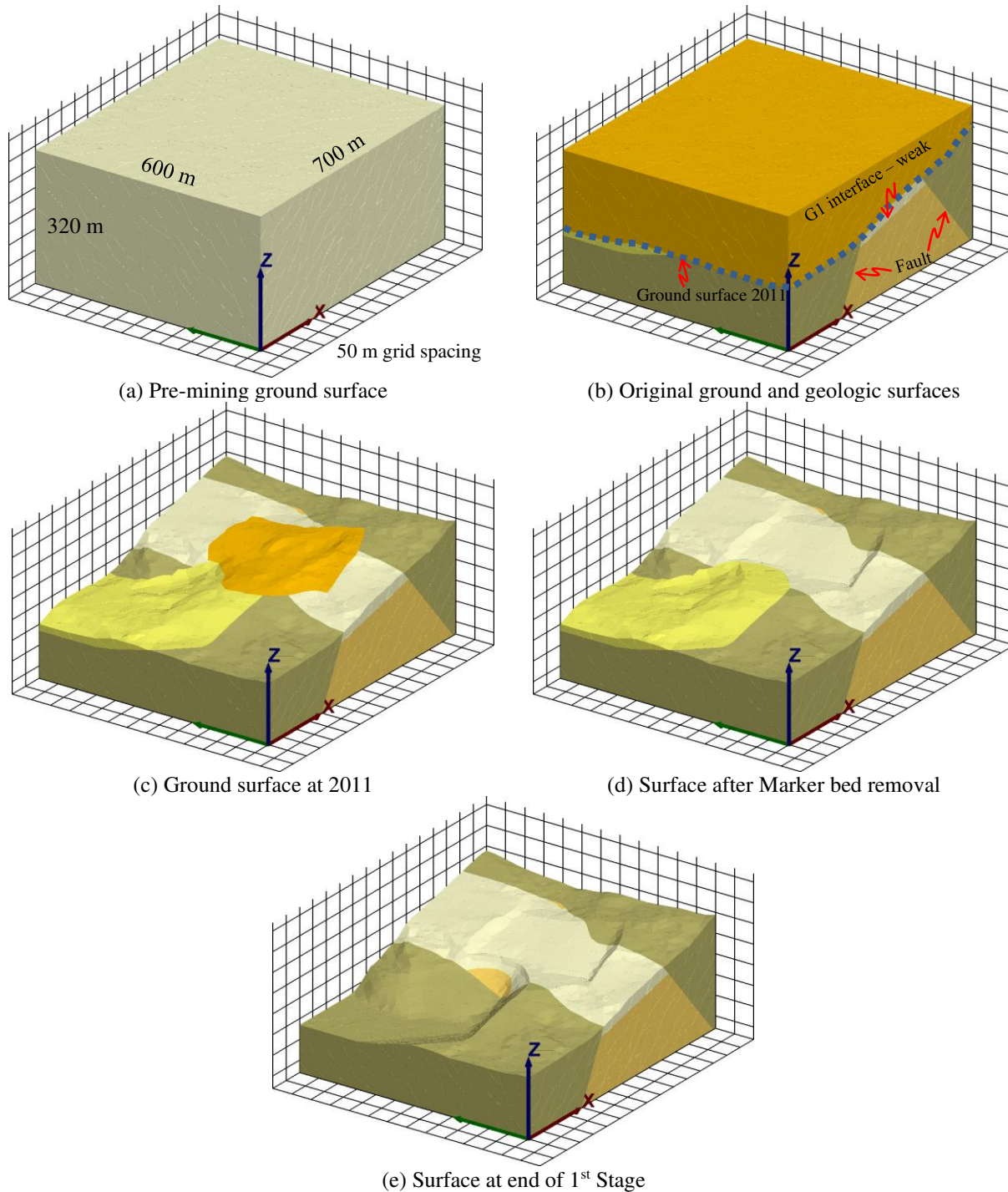
(a) Pre-mining ground surface

(b) Original ground and geologic surfaces

(c) Ground surface at 2011

(d) Surface after Marker bed removal

(e) Surface at end of 1st Stage

Figure 17. Pre-mining ground surface, topographic, and major geologic structure surfaces in model.

After the generation of the mesh and surfaces, the model was discretized to obtain a number of tetrahedral elements or zones. The average edge length of the tetrahedral zones was 10 m. The physical properties of the underburden claystone rock mass were assigned to all the tetrahedral zones in the model; these physical properties were tabulated earlier in Table 1.

The boundary conditions of the model were assigned as rollers on all side walls and the bottom of the model. The zones were sequentially deleted from the model to simulate the sequential excavation. From Figures 17(b) to 17(e), a sequential excavation was performed to obtain the topographic surface of Year 2011, the Marker bed removal, and the end of the 1st

Stage surfaces. At the end of the 1st Stage, the G1 interface was clearly daylighted in the undercut slope face (between the light yellow and gold blocks in Figure 17(e)). For each step of the excavation, the model was run to meet its equilibrium state, and the displacements and stresses were examined later on.

Initial Horizontal Stress

The Mae Moh deposit consisted of a major geologic structure which was a set of normal faults. The strike of the faults was aligned in the north - south direction. The borehole observation using televiewers was not one of the mine engineers' options. The pit mapping was mainly utilized for collecting all observed geologic structures in the Area 4.1 by the mine's geologists. To understand the effect of the initial stress on the numerical model, the initial horizontal stress conditions of the model were varied. The variations in horizontal stress in terms of lateral earth pressure coefficients, or k_x and k_y, are listed in Table 2. The directions of k_x and k_y were perpendicular and parallel to the fault's strike in the numerical model, respectively. The value of k_x is always less than k_y because the direction of k_x is the same as the minimum compressive stress. The initial horizontal stress conditions were set at the beginning of the model (Figure 17(a)). After the original ground surface was excavated to ground surface 2011, the values of k_x and k_y were increased. Particularly in the zones near the ground surface, the coefficients soared considerably.

Figure 18 presents k_x and k_y with the depth along the vertical center line of the model. The depth of the model was measured from the top of the big block (blue dot). Near the free face, the values for both k_x and k_y of the zones were much greater than those assigned. They continuously converged to the initially assigned horizontal stresses with depth.
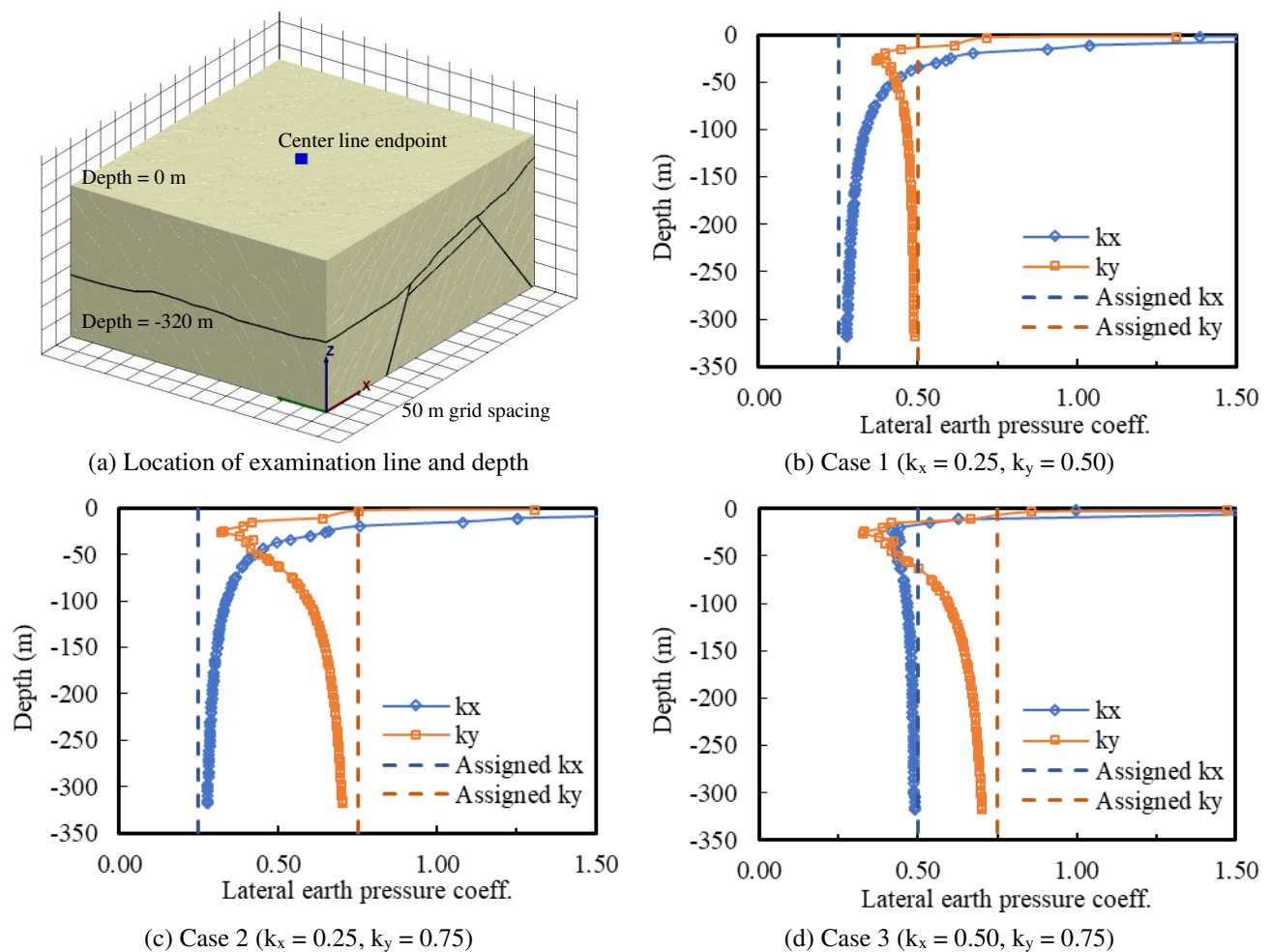

(a) Location of examination line and depth

(b) Case 1 ($k_x = 0.25$, $k_y = 0.50$)

(c) Case 2 ($k_x = 0.25$, $k_y = 0.75$)

(d) Case 3 ($k_x = 0.50$, $k_y = 0.75$)

Figure 18. Lateral earth pressure coefficients and depth at original ground surface.

Table 2. Variations in initial horizontal stress condition.

Case	k_x	k_y	Maximum displacement, Δ_{max} (m)	FS
1	0.25	0.50	0.411	1.15
2	0.25	0.75	0.496	1.21
3	0.50	0.75	0.463	1.28

Figure 19 also presents the coefficients with depth after the original ground surface was excavated to ground surface 2011. Initial coefficients k_x and k_y are both seen to have increased by quite a fair amount. The lateral earth pressure coefficient in the x direction (k_x) increased from 0.25 to 0.50 in Cases 1 and 2 and rose slightly in Case 3. The values for k_y also increased approximately 0.125 from their initial values in all cases.
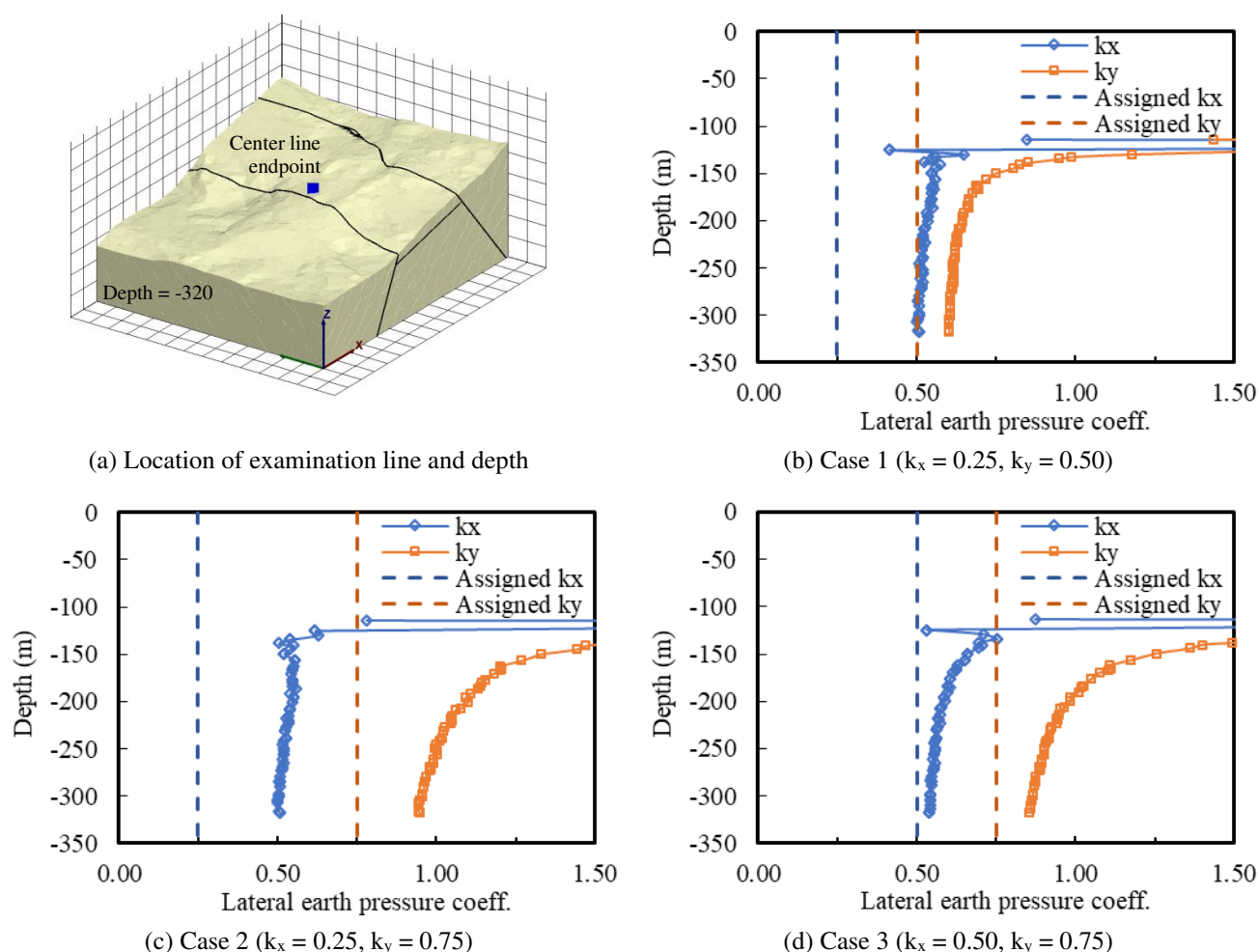

(a) Location of examination line and depth

(b) Case 1 ($k_x = 0.25$, $k_y = 0.50$)

(c) Case 2 ($k_x = 0.25$, $k_y = 0.75$)

(d) Case 3 ($k_x = 0.50$, $k_y = 0.75$)

Figure 19. Increase in lateral earth pressure coefficients and depth at ground surface 2011.

Effect of Initial Horizontal Stresses on Undercut Slope Model

The sequential excavation was continued after the big block model was excavated to ground surface 2011 by the removal of the Marker bed and the undercutting. After the undercutting, the maximum total displacements were in the same location at the potential sliding block's slope face, near the G1 interface (Figure 20). The displacements decreased with the distance

away from the slope face. The regions above the pillars also showed less displacement. The maximum total displacements and the factors of safety were narrowly different and fell in the range of 0.411 m - 0.496 m and 1.15 - 1.28, respectively.

From Table 2, it is seen that an increase in the total displacement is not necessarily the cause of the decrease in the factor of safety or vice versa if the initial stress is different. Case 3 is added for consideration. Despite all the cases sharing the same boundary conditions, the initial stress for each case is different due to the values of k_x and k_y.

The comparative level of isotropic confining stress, indicated by $(k_x+k_y)/2$, was consistent with the factor of safety; i.e., the more confining stress, the better stability. Although the factor of safety value was supposed to decrease as the model became less stable, due to the increase in total displacement, the trajectory and reorientation of the principal stress can also affect the maximum displacement of the potential sliding block near the undercut slope face.
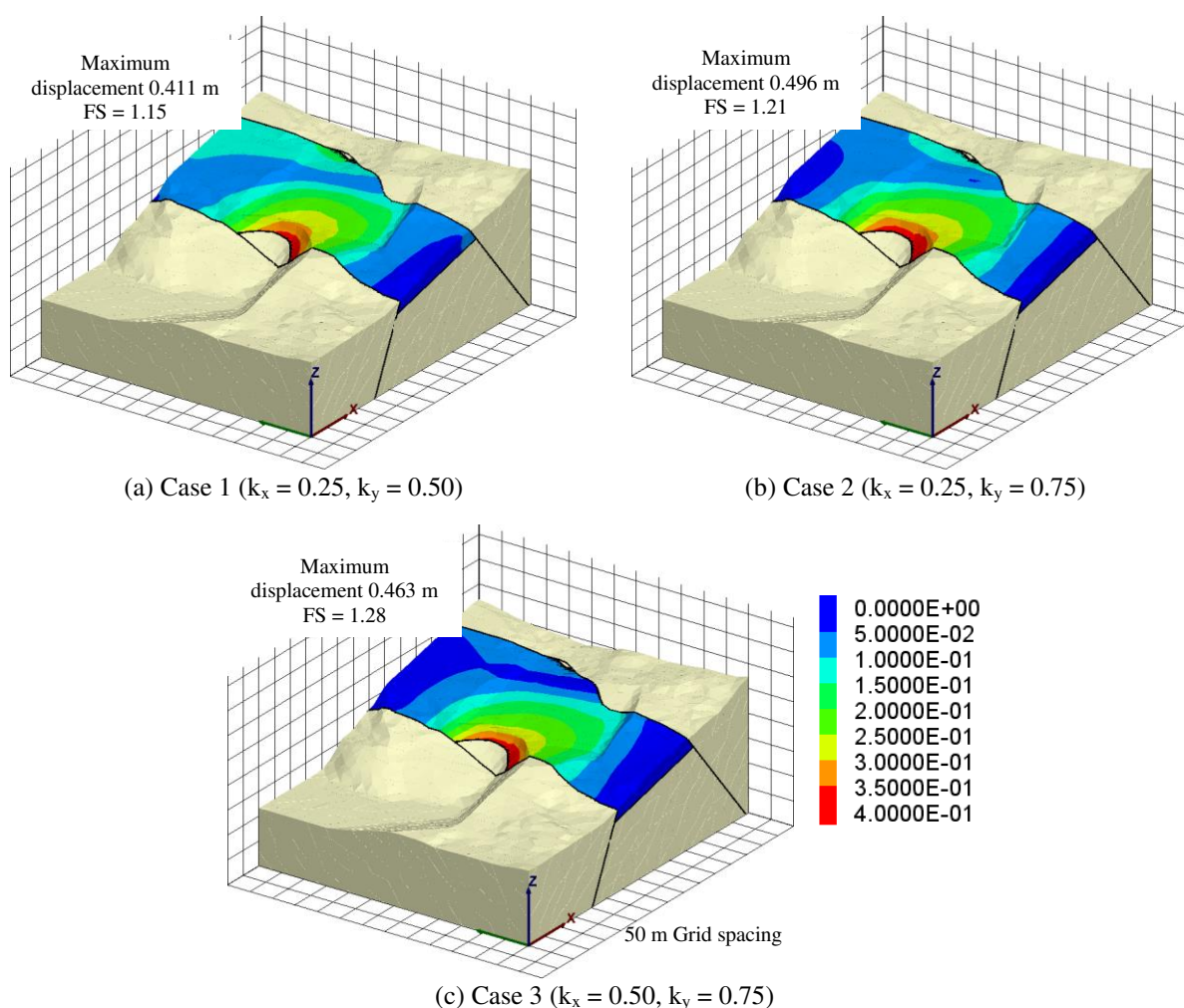

(a) Case 1 ($k_x = 0.25$, $k_y = 0.50$) (b) Case 2 ($k_x = 0.25$, $k_y = 0.75$)

(c) Case 3 ($k_x = 0.50$, $k_y = 0.75$)

Figure 20. Maximum total displacements of undercut models.

The principal stress trajectories of the models are plotted in Figure 21. The positive stress indicates the compressive stress. The direction of the maximum compressive stress is obviously aligned in the tangential direction to the excavation in all cases. The magnitude of the maximum compressive stress in Case 1 was the least. The magnitudes of the maximum compressive stress were apparently similar in Cases 2 and 3. The total displacement contours and principal stresses of all the cases clearly showed arching in the potential sliding block, similar to the simple model. As the total displacements for all cases were slightly different, Case 1 was selected as the case for more undercut slope behavior investigations of Area 4.1.
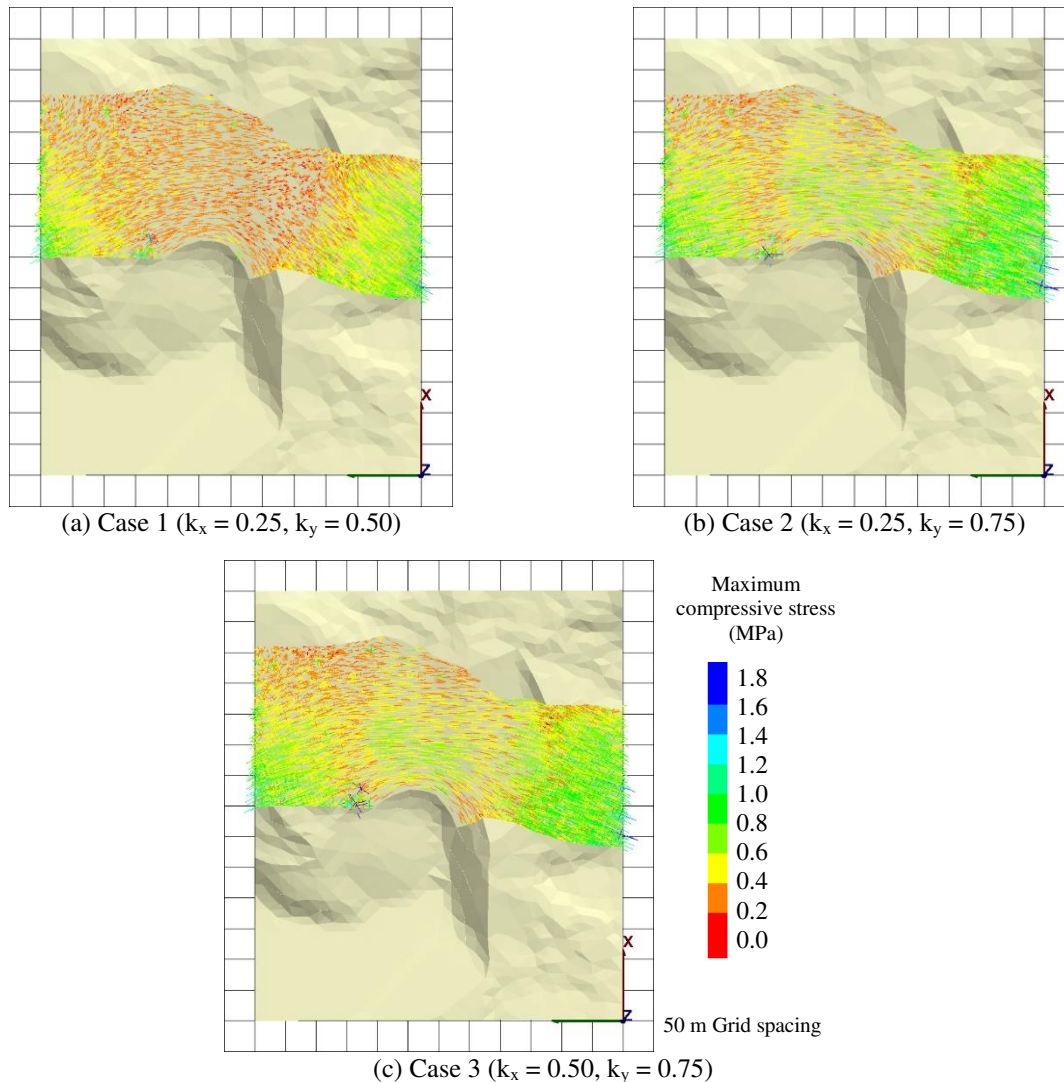
(a) Case 1 (k_x = 0.25, k_y = 0.50)

(b) Case 2 (k_x = 0.25, k_y = 0.75)

Maximum compressive stress (MPa)

1.8
1.6
1.4
1.2
1.0
0.8
0.6
0.4
0.2
0.0

50 m Grid spacing

(c) Case 3 (k_x = 0.50, k_y = 0.75)

Figure 21. Principal stress trajectories in potential sliding block of undercut models.

COMPARISON OF DISPLACEMENTS BETWEEN MONITORING DATA AND NUMERICAL MODEL RESULTS

Comparison of Surface Displacements between Monitoring Data and Numerical Model Results

As presented in Figure 20(a), the maximum displacement was 0.411 m and it was located at the potential sliding block's slope face, near the G1 interface. In Figure 22, the displacement contours were overlaid with displacement vectors. The vectors showed an unusual upward displacement component. However, the upward displacement near the undercut face went undetected by the Robotic Total Station in the field. It is very likely that the upward displacement vectors were caused by the massive excavation involving the Marker bed removal and the undercutting steps or model unloadings.

Based on the simple numerical model, the undercut slope displaced along the weak or sliding plane. Therefore, the displacement vectors of the 13 nodes located near the prisms were utilized to obtain the magnitudes of the tangential displacement vectors at the G1 interface plane (sliding plane). Tangential vector v_t of vector v at a plane is depicted in Figure 23. The normal vector or the pole of the G1 interface, an essential input for determining the tangential displacement vector, was calculated and equaled 087.8º/75.7º (Trend/Plunge). The normal vector of the G1 interface was the mean normal vector of the G1 interface faces, which were extracted from the numerical model.
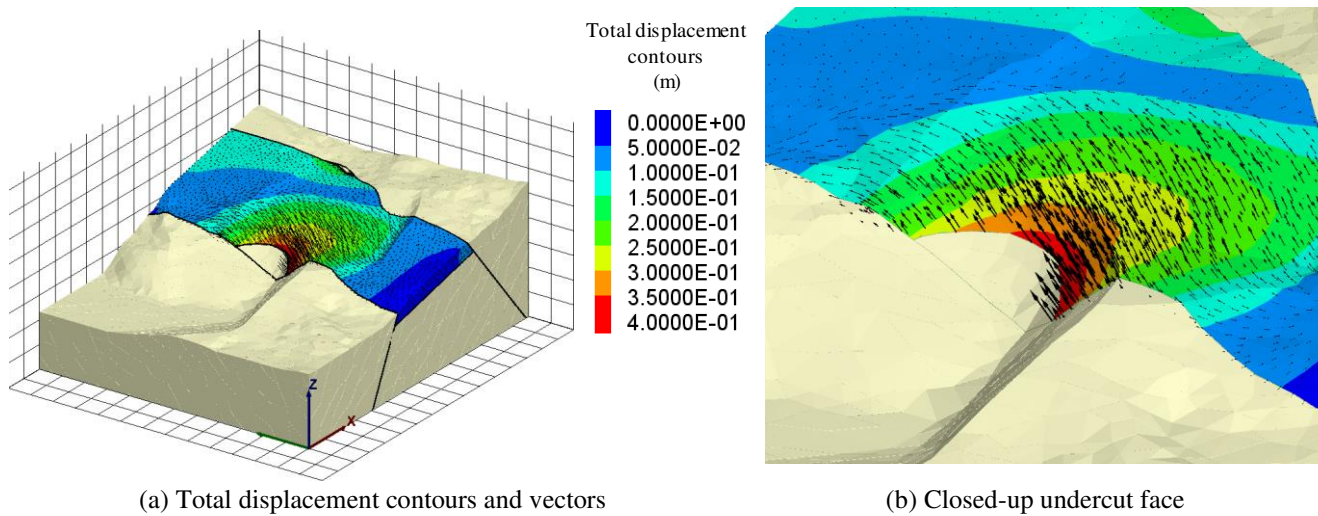
(a) Total displacement contours and vectors   (b) Closed-up undercut face

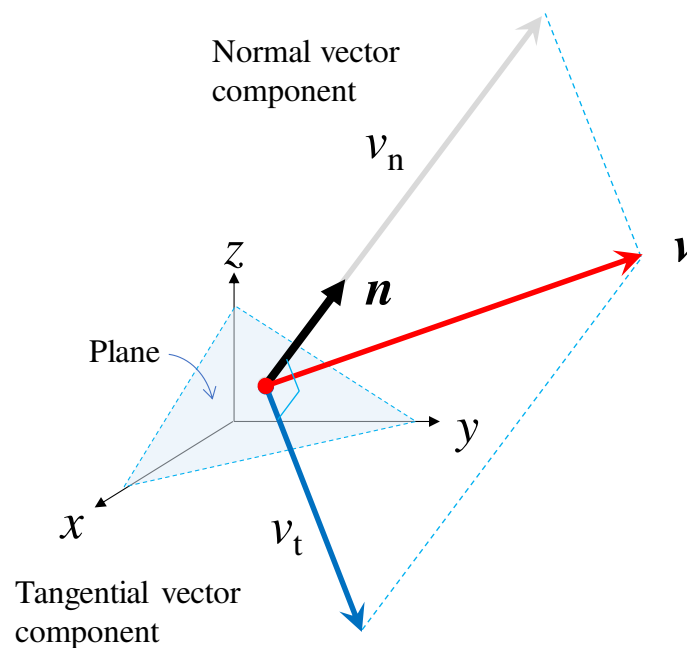*Figure 22. Total displacement contours and vectors of undercut model.*

Figure 23. Tangential vector of a given vector at a plane.

Figure 24 presents the surface displacement plot using the monitoring data, total displacements, and magnitudes of tangential displacement vectors at the G1 interface plane from the numerical model. The total displacements from the numerical model were fairly comparable to those of the monitoring data. The total displacements from the numerical model at SD15, SD16, and SD17 were quite a bit larger than those of the monitoring data. The locations of SD15, SD16, and SD17 were at the Mid Floor and thus not far away from the undercut face.

The total displacements from the numerical model and the magnitudes of tangential displacement were slightly different in the Upper Floor. However, they were incomparable in the Mid and Lower Floors. These floors were located near the excavation, and the nodes around them tended to have the upward displacement component in the numerical model.
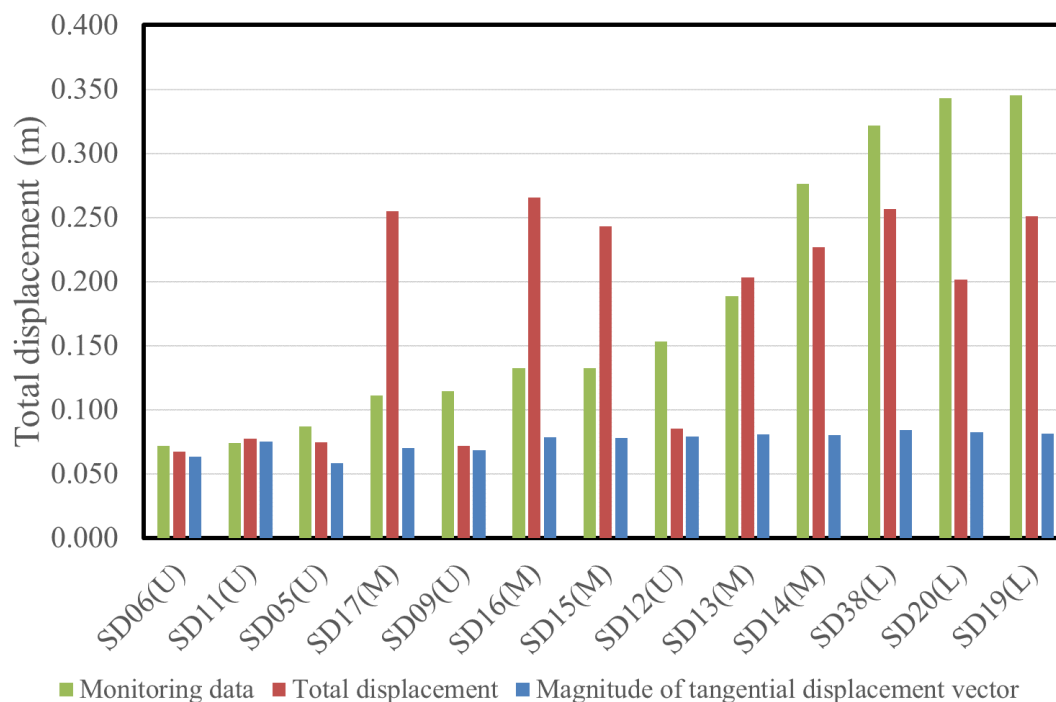
Figure 24. Comparison of surface displacements.

Another comparison of the surface displacements was done for the surface displacements measured by the inclinometers. The surface displacements measured by the inclinometers did not include any vertical displacements. The surface displacements were the horizontal displacements of the borehole collar. The measured borehole collar displacements are tabulated in Table 3. The displacement vectors of the nodes near the inclinometers from the model are also listed in Table 4. To compare the horizontal displacements between the model and the measurements, the horizontal vectors of the nodes near the inclinometers and the borehole collar displacements were drawn together. The horizontal displacements of I203, between the measurements and the numerical model, were comparable both in magnitude and direction. The horizontal displacements from the numerical analysis and the measurements were much different at I192 and I29.

According to Figure 15, although the potential sliding block above the daylighted G1 interface obviously moved along the G1 interface, a slight shear deformation was observed in the underlying rock mass and the potential sliding block. Therefore, the magnitude of the movements observed in Figure 25 is always larger than that of Figure 26 and their difference represents the shear deformation of the potential sliding block.

Table 3. Borehole collar displacement.

Inclinometer	A axis		B axis		Transformed to model coordinate				
	Azimuth	Collar displacement (m)	Azimuth	Collar displacement (m)	Δv_x (m)	Δv_y (m)	Δv_z (m)	Horizontal displacement magnitude (m)	Displacement direction (º)
I192	80	-0.0208	170	-0.0172	-0.0065	0.0262	NA	0.027	256.0
I203	80	-0.0715	170	0.0660	-0.0967	-0.0107	NA	0.097	173.7
I29	70	-0.0116	160	-0.0081	-0.0067	0.0124	NA	0.014	241.4

Table 4. Displacement vectors and magnitudes of nodes near inclinometers.

Inclinometer	Displacement vector			Horizontal displacement magnitude (m)	Displacement direction (°)
	Δv_x (m)	Δv_y (m)	Δv_z (m)		
I192	-0.1128	0.0110	0.2051	0.113	185.6
I203	-0.1167	0.0298	0.1243	0.121	194.3
I29	-0.0636	0.0035	-0.0425	0.064	183.2
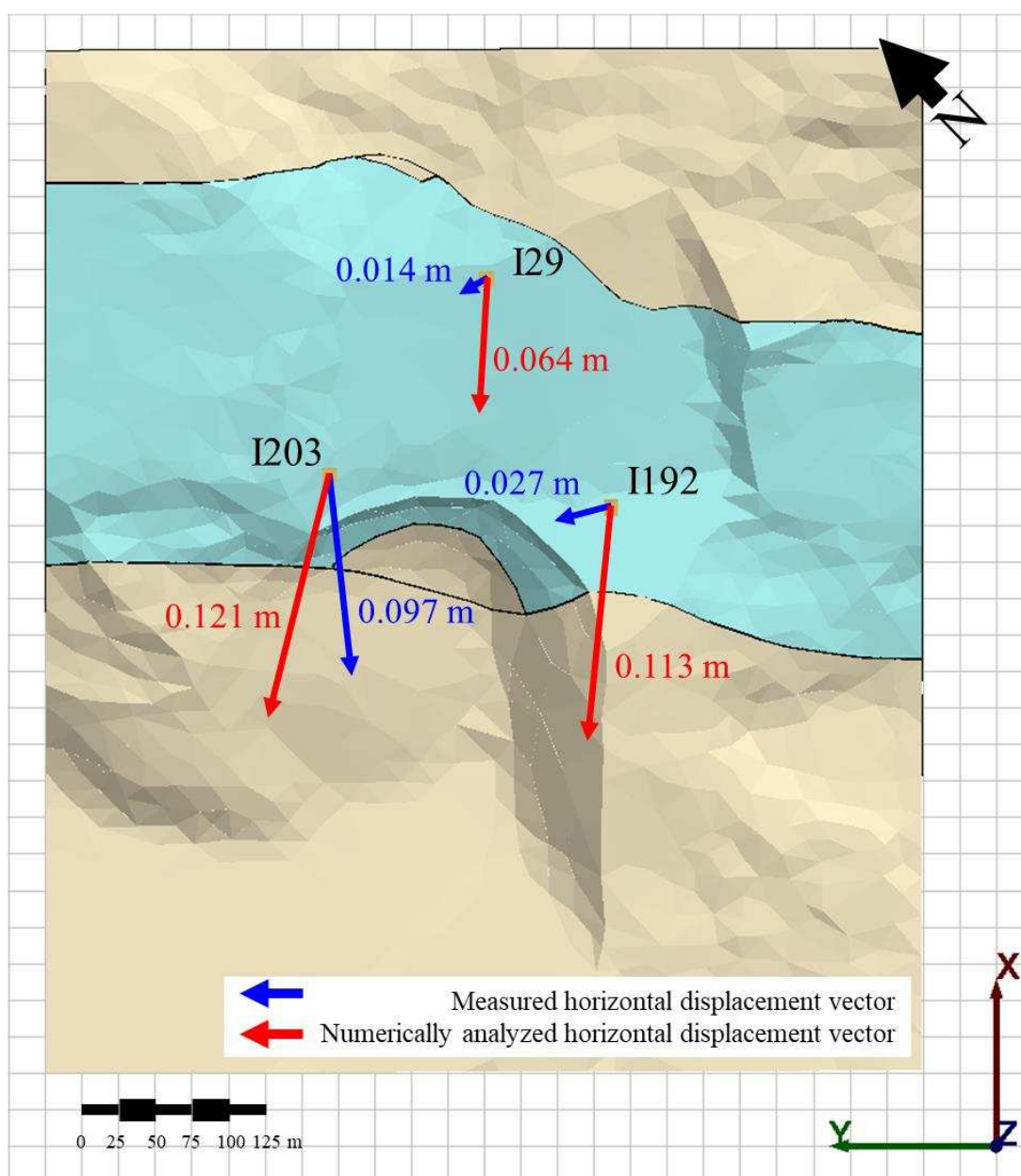
Figure 25. Horizontal displacements of inclinometer collars.

Comparison of Subsurface Displacements between Monitoring Data and Numerical Model Results

The subsurface displacements measured by the three inclinometers were summarized and compared with the results of the numerical analysis. The subsurface displacements measured by the inclinometers are presented in Table 5, and the displacement vectors of the nodes at the G1 interface, near the subsurface measurements, from the model, are shown in Table 6. It is seen from the inclinometer data that the greatest magnitude of subsurface displacement was measured by I203 because I203 was placed closest to the undercut face. The subsurface displacement measured by I192 was quite a bit smaller than that measured by I203. I192 was placed in the pillar of the undercut slope. The subsurface displacement directions of I192 and I203 were almost parallel (the X-axis in the model). The subsurface displacement measured by I192 was slightly larger than that measured by I29. The subsurface displacement measured by I29, in the Upper Floor, was the farthest from the undercut face and therefore showed the lowest magnitude.

The subsurface displacements from the numerical analysis on the nodes near the inclinometers fell in the range of 0.001 m to 0.052 m. The subsurface displacement vectors by the inclinometers and the numerical analysis are graphically shown in Figure 26. The subsurface displacements are comparable to the measured ones only for I203. The subsurface displacements near the undercut face, between the inclinometer data and the numerical model, in terms of direction and magnitude, were comparable. For the area farther away from the undercut face, the subsurface displacement directions and magnitudes were unmatched. It is concluded that the complexities of a site's geology could be one of the major challenges of numerical modelings.

Table 5. Subsurface displacements measured by inclinometers.

| Inclinometer | A-axis | | B-axis | | Transformed to model coordinate | | | | |
	Azimuth	Collar displacement (m)	Azimuth	Collar displacement (m)	Δv_x (m)	Δv_y (m)	Δv_z (m)	Horizontal displacement magnitude (m)	Displacement direction (°)
I192	80	-0.0135	170	0.0081	-0.0156	0.00149	NA	0.016	185.4
I203	80	-0.0612	170	0.0630	-0.0866	-0.0144	NA	0.088	170.5
I29	70	-0.0011	160	-0.0097	0.00332	0.0091	NA	0.010	289.9

Table 6. Displacement vectors of nodes at G1 interface from numerical analysis.

| Inclinometer | Displacement vector | | | Horizontal displacement magnitude (m) | Displacement direction (°) |
	Δv_x (m)	Δv_y (m)	Δv_z (m)		
I192	-0.0011	0.0004	-0.0002	0.001	201.2
I203	-0.0343	-0.0195	-0.0078	0.039	150.4
I29	-0.0509	-0.0119	-0.0130	0.052	166.8

NUMERICAL MODEL OF 2nd STAGE OF AREA 4.1

The 2nd Stage of the Area 4.1 undercutting was numerically modeled for the Class B prediction (analysis done during the construction), based on the mine plan, as previously described. The numerical model for the 2nd Stage of Area 4.1 was revised by expanding its dimensions to cover the additional mining area, including the extended geologic structure surfaces. The 2nd Stage model initially consisted of 429,964 elements and 335,764 nodes for modeling 11 huge deformable blocks, reflecting three geologic structures and three mining surfaces. Figures 27(a) and (b) present the excavation direction, based on the mine plan. The number of elements and nodes of the 2nd Stage model were less than the 1st Stage model because the block above

the pit wall surface was discretized coarsely for a shorter time calculation. However, the material properties remained unchanged.

The displacement and stress trajectory plots for the numerical model clearly show the existence of arching in the potential sliding block, as presented in Figures 27(c) and 28. The maximum displacement was 0.715 m and it was located near the G1 interface. The numerical model was applied additionally to calculate the safety factor at the end of the 2nd Stage using the popular Shear Strength Reduction technique. The safety factor of the model was reportedly 1.07.

In October 2017, all mining activities of the 2nd Stage were successfully completed without any casualties. Area 4.1 and the vicinity became a restricted area of the mine. A year later, the displacement of the restricted Area 4.1 immediately spiked during the rainy season of 2018. The mine and all the mine staff actively responded and were well prepared for the failure of the rattling Area 4.1. At the end of October 2018, part of the undercut slope of Area 4.1 (Figure 29) failed between the backfilling of the 1st and 2nd Stages (see Figure 13(c)). The failure extended from elevations of 104 msl and 192 msl, and was approximately 200 m in width. The width of the failure was as wide as the length of the daylighted G1 interface at 190 m. Therefore, the preliminary study giving the maximum undercut width of 150 m (see Figure 8(f)) confirms that the proposed analyses (Class A predictions for the 1st Stage and Class B predictions for the 2nd Stage) are on the safe side.

The slope failure in the field (Figure 29) is shown as a vertical shear plane and is evidence of the rock mass failure on the side of the sliding block (side resistance), also called flank. However, the failure of the rock mass of the block was hardly captured by the numerical model in this study because of the complexity of the geologic structures in Area 4.1. In fact, the results of one case of failure would not be sufficient to confirm other unknown multiple variables. Later, Area 4.1 was treated as an abandoned mining site; therefore, there was no further investigation of this failure.
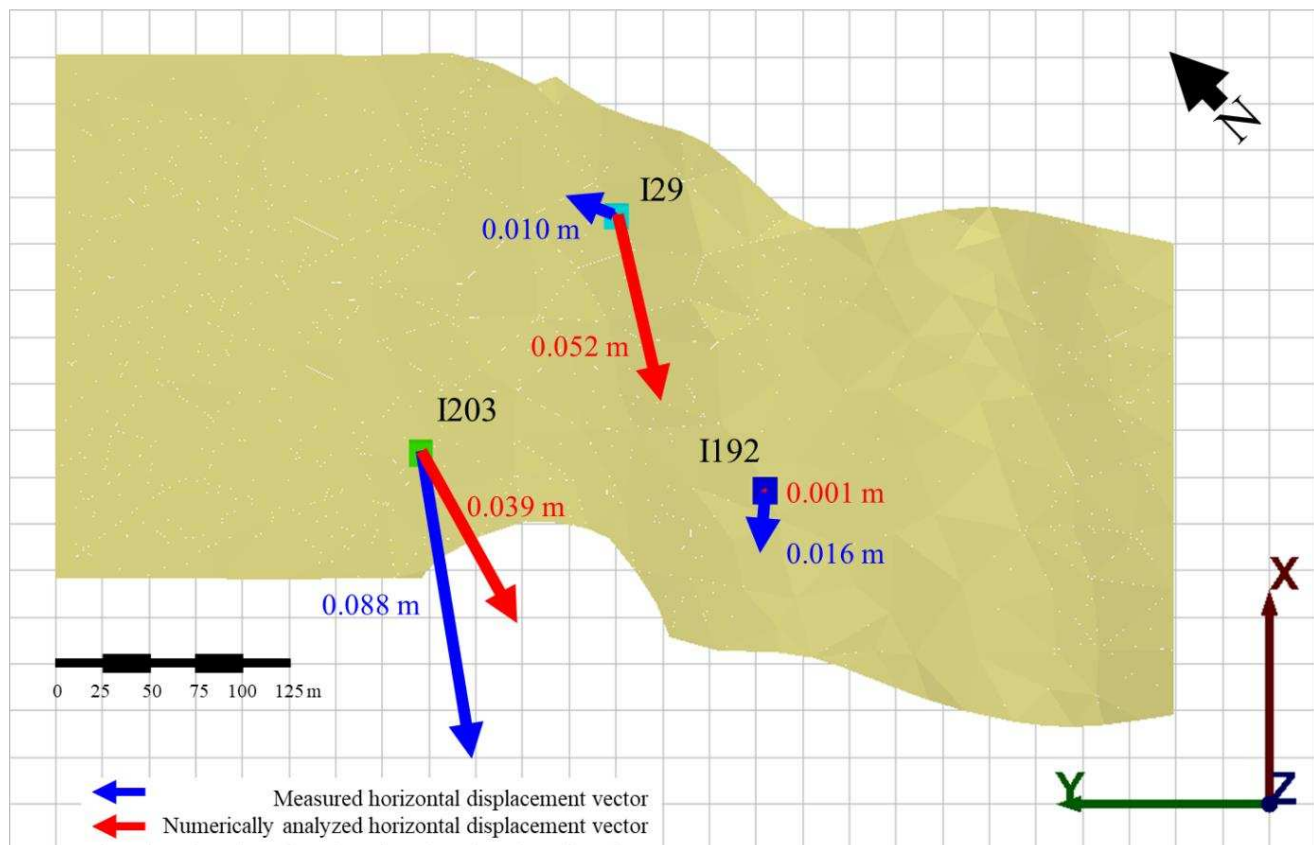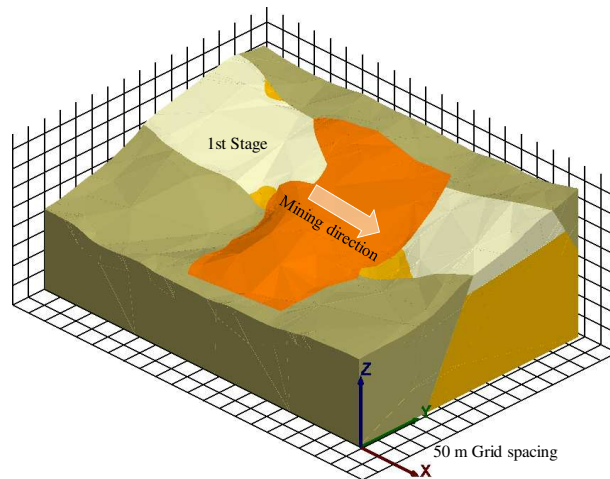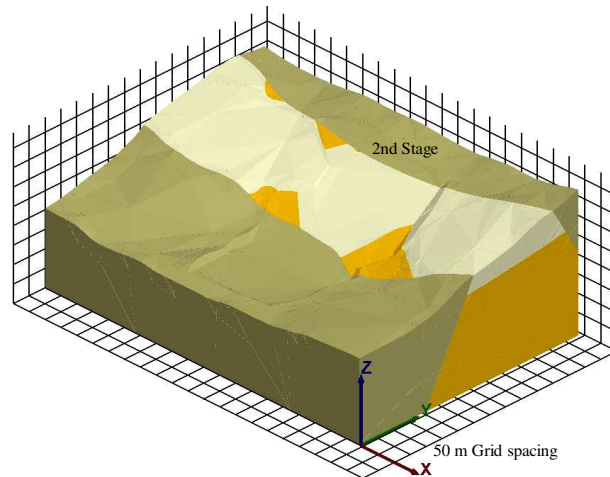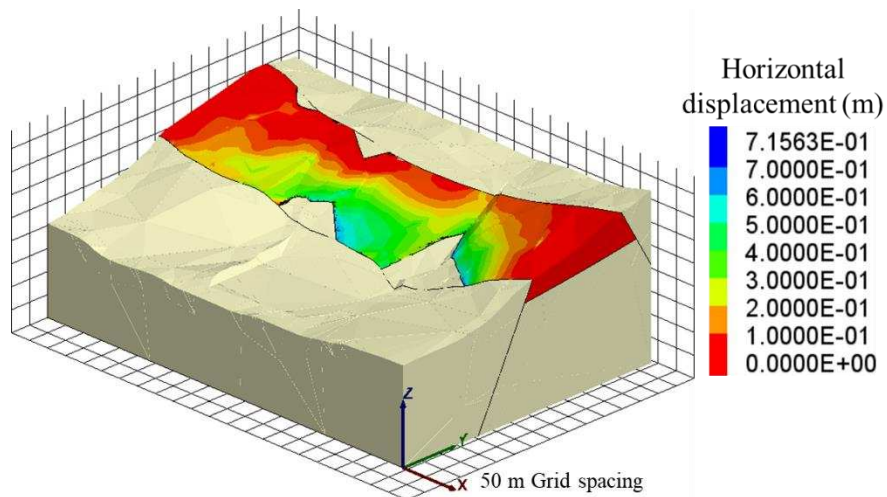

Figure 26. Subsurface displacements of inclinometer at G1 interface.

(a) At beginning of 2nd Stage

(b) At end of 2nd Stage

(c) Horizontal displacements of undercut slope model in G1 interface's dip direction

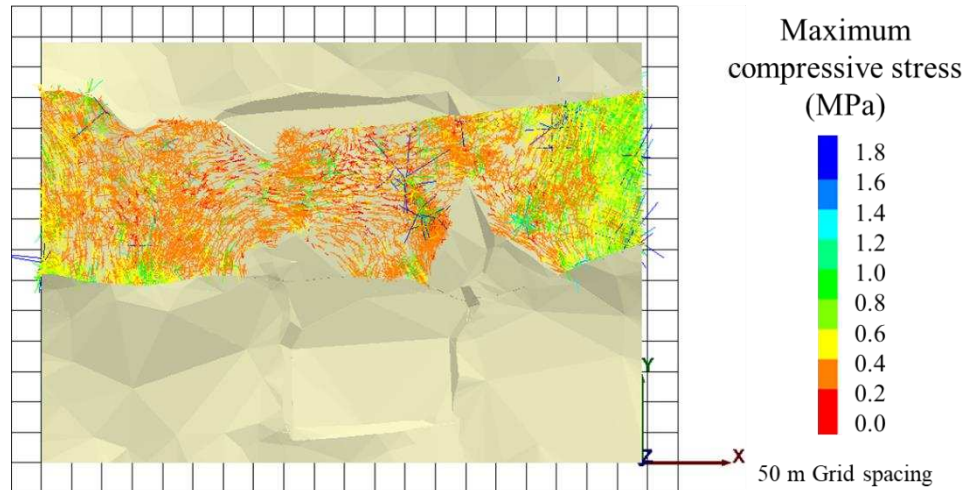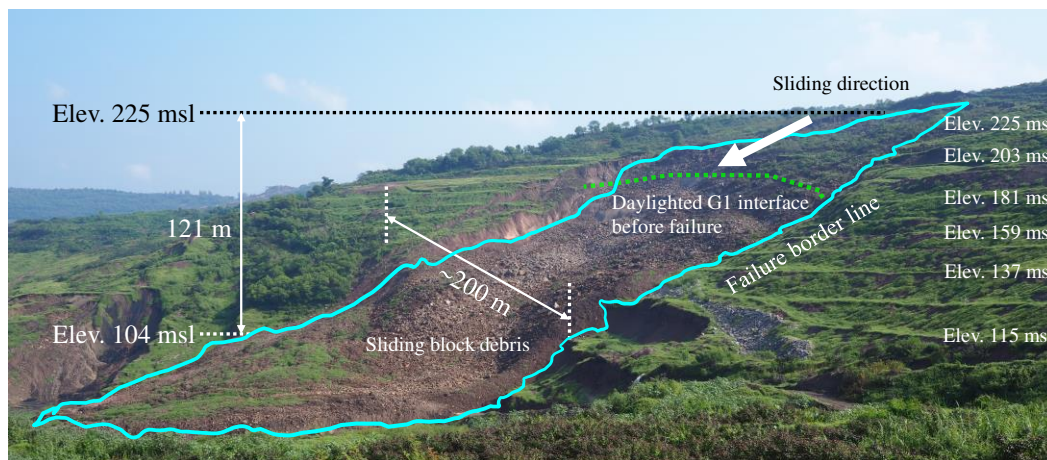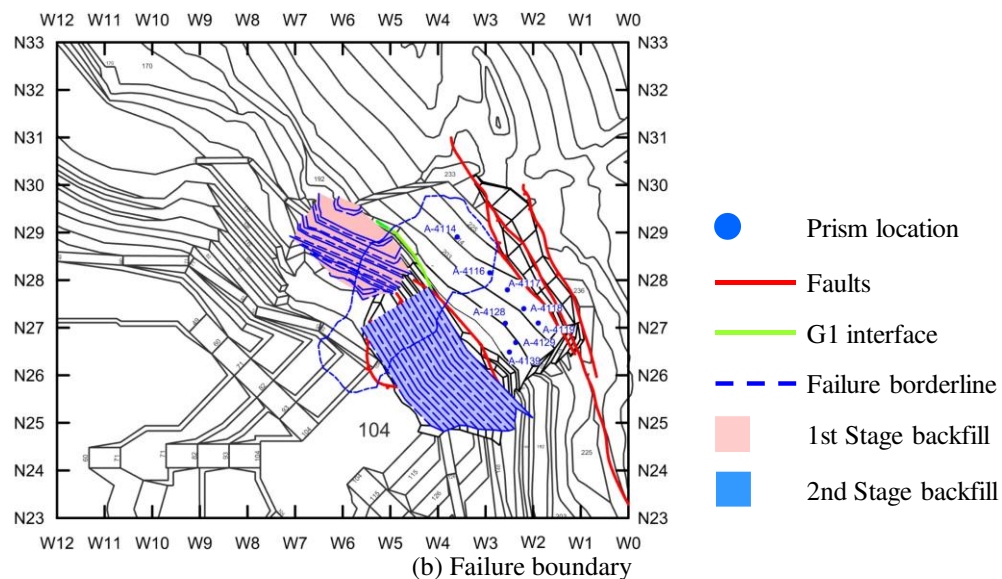*Figure 27. 2nd Stage numerical model and its horizontal displacements of undercut.*

Figure 28. Principal stress trajectories in potential sliding block of 2ⁿᵈ Stage.

(a) Photo of Area 4.1 failure

(b) Failure boundary

Figure 29. Area 4.1's debris after failure in October 2018.

MONITORING DATA OF 2nd STAGE OF AREA 4.1

As stated earlier, the monitoring data gathered during the undercutting of the 2nd Stage was unfortunately damaged, but partially recovered. Thus, comparative data between the numerical analyses and the field measurements will be presented. The recovered monitoring data of the 2nd Stage, which were the surface displacements from eight prisms, are presented in this section. Figure 30 shows the surface displacement data between March 2015 and February 2016, and between June 2018 and October 2018.
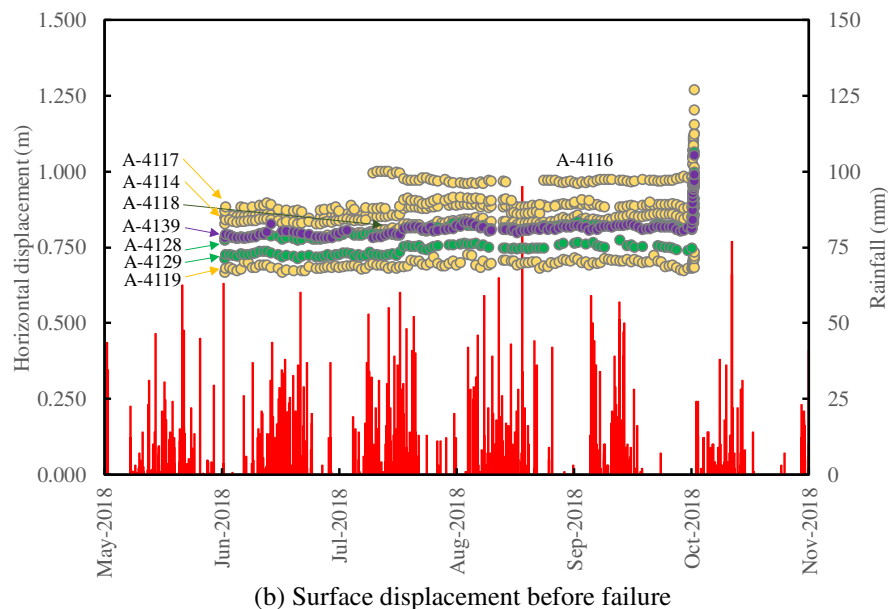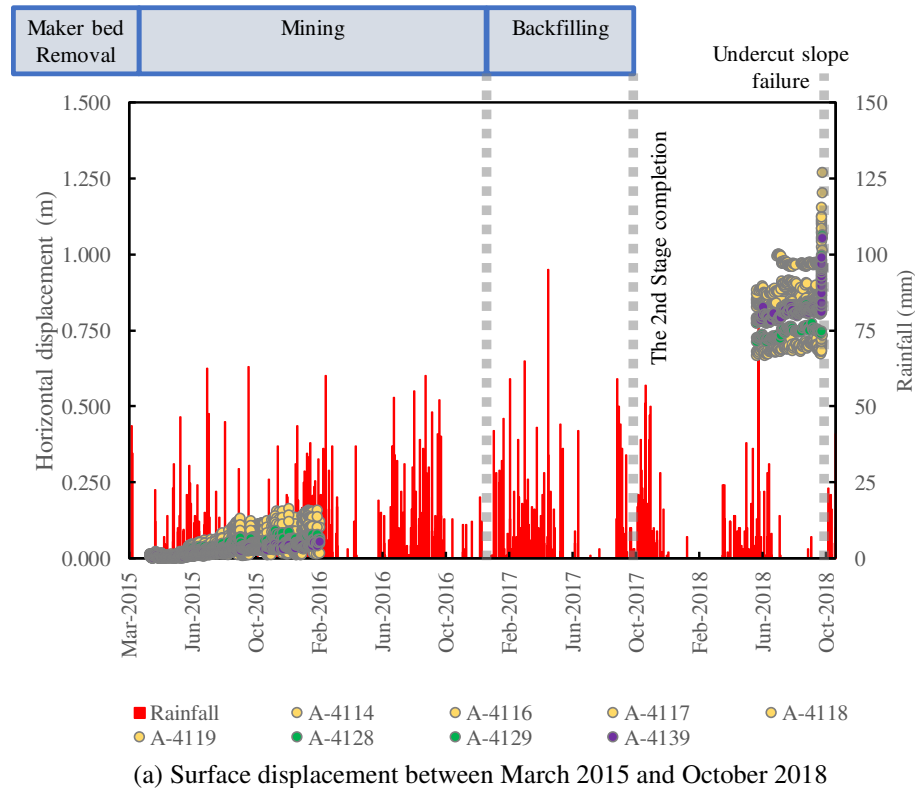

(a) Surface displacement between March 2015 and October 2018

(b) Surface displacement before failure

Figure 30 Surface displacement of 2nd Stage of Area 4.1.

As planned, the prisms were additionally installed in the 2nd Stage of Area 4.1 after the Marker bed had been excavated. After the installation, the potential sliding block continuously displaced because of the mining activity and additional undercutting in Area 4.1 (Figure 30(a)). The surface displacement pattern of the potential sliding block in the 2nd Stage was similar to that of the 1st Stage. The area near the undercut face displaced more greatly than the area far away from the undercut face. Unfortunately, the surface displacement data from February 2016 to the end of the 2nd Stage are missing, but became available in the next rainy season between June and October 2018, before the failure (Figure 30(b)).

After the undercutting and before the failure, all the available surface displacement data showed that the potential sliding block had the accumulative surface displacement of approximately 1 m and rapidly displaced on the day of failure. The surface displacements from the monitoring data, one day before the failure, are plotted with the surface displacement of the numerical model of the 2nd Stage in Figure 31. The surface displacements of the numerical model were incomparable. The displacement magnitudes of the monitoring data were much larger than those of the numerical model.
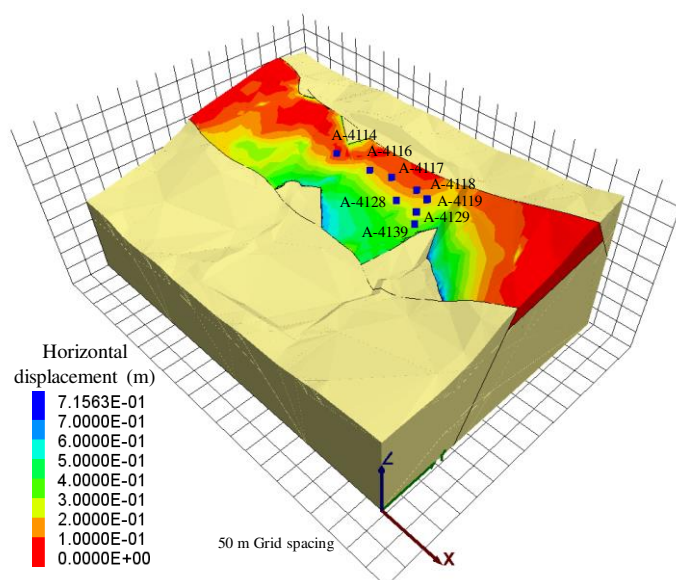
(a) Location of prisms in model
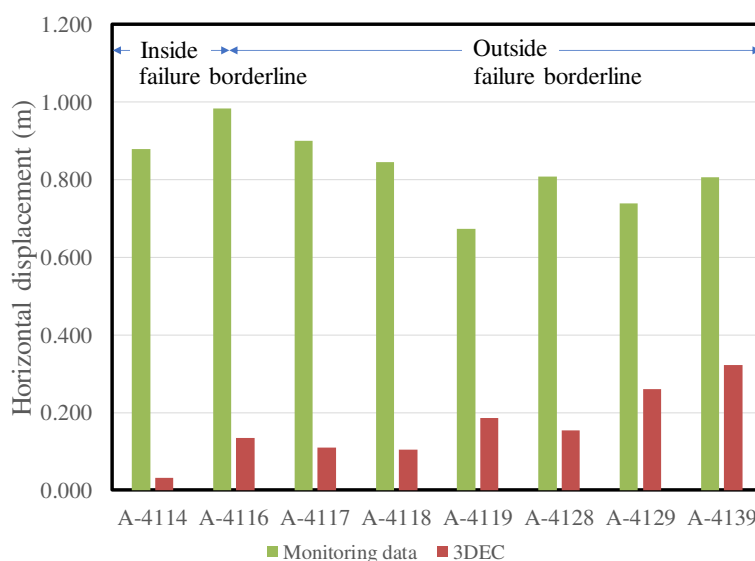
(b) Surface displacements

Figure 31 Comparison of surface displacements at 2nd Stage of Area 4.1.

To confirm the strength parameters used in the numerical analysis, further investigations of the failure would be an excellent back analysis case study. The authors plan to conduct Class C predictions (analyses taken after the construction) for the subsequent papers as water pressure in the G1 interface, which has a significant impact on the stability of undercut slopes.

For the design and plan of Area 4.1, numerical analyses were an important tool for connecting theory and practice. The engineers were able to add or replicate the complexities of the boundary conditions, geology, and mine designs to the numerical models. The results of the numerical analyses provided more insights into the behavior of undercut slopes for engineers. Moreover, the results will be of potential use in the evaluation of mine designs. Conclusively, the mine plans and operation of Area 4.1, applying the arching effect as a temporary support, were an example of a successful case in Thailand's mining history in terms of enormous undercut slopes. This undercutting technique helped to slash costs of the overburden removal while successfully maintaining sufficient safety for the mine operations to continue. As a result, the mineable reserves were increased and mining projects have become more attractive, feasible, and sustainable. The undercutting technique is undoubtedly an attractive and practical option for open-pit mine projects.

DISCUSSIONS

The assumptions used in the numerical models and the failure mechanisms observed at the actual site are listed as follows:

1. Creep behavior, weathering beyond the exposed surface, poor drainage, and progressive failure were observed in their actual conditions. Therefore, the assumptions used in the numerical models were hardly satisfied, resulting in some discrepancies between the measurements and the predictions.

2. Due to the assumption of fully functioning drainage, the analyses were undertaken without giving consideration to the seepage or uplift force. Therefore, the mechanisms of undercut slope failure occurring in the rainy season could not be captured by the numerical models.

3. Since the actual failure of the undercut slope involved both the collapse of the claystone rock mass on the slope and the large slippage of the G1 interface, the assumption of the simultaneous shear strength reduction employed in the determination of the factor of safety is reasonable.

4. The numerical models can capture the actual failure mechanisms induced by the sequential excavation in which the accumulative deformations gradually destabilize the undercut slope.

5. In the 1st Stage of Area 4.1, the stability observed by the numerical model and that observed at the actual site were consistent. Therefore, the assumptions in the numerical model might not be excessively different from those at the actual site. The factor of safety of 1.15 obtained from the numerical model of the 1st Stage of Area 4.1 implies that the undercut slope would be able to endure a slight uplift force generated in the G1 interface as well as a slight extent of weathering in the claystone rock mass. Essentially, the undercut slope was favorably stable for the period of the 1st Stage because a system of horizontal drainage was installed to effectively reduce all the water pressure in the G1 interface. Thus, the effective friction angle at the G1 interface was seemingly intact.

6. For the 2nd Stage, the factor of safety was 1.07 because of the wider undercut width. After the cut-and-fill in the 2nd Stage had been completely done, Area 4.1 was abandoned and restricted. The maintenance of the horizontal drainage system was also neglected and finally malfunctioned. With the water pressure in the interface, the undercut slope stability was jeopardized and the undercut slope lasted only one rainy season. Therefore, the assumption of the numerical models, on the water pressure in the G1 interface and the rock mass strength of the potential sliding block, captured and matched the undercut slope behavior at Area 4.1.

7. The behavior of the undercut slope was fairly well captured by the numerical model in terms of the surface and subsurface displacements. The directions of the surface and subsurface displacements from the numerical model were comparable to those of the monitoring data, using the prisms and the inclinometers (Figures 25 and 26). Their magnitudes, however, were incomparable (Figures 15, 16, 24, 25, and 26). The displacements from the instruments in the field were larger than the numerical model results.

8. It should be noted that the full capability of the software was not utilized in this study because the rock mass was assumed as a continuum body and the boundary conditions of the slope model did not allow the blocks to slide and

detach kinematically. More realistic analyses could be achieved by adding geologic structures to the rock mass, such as joints, but more computing resources would be required for compensation. In such cases, the rock mass would consist of a number of discrete blocks by which the model could consequently show rotations and structurally controlled failures.

CONCLUSIONS

The academic contribution of this study is the application of a numerical analysis for the novel undercutting method by which geological coal resources can be turned into minable reserves or the mineable reserves of a particular deposit can be increased along with the profitability of the mining project.

Undercut slope behaviors were initially studied in laboratories via physical and theoretical models. In the present study, to determine the suitable undercut width for Area 4.1, three-dimensional numerical analyses were utilized. A simple numerical model was constructed and the stability of an undercut slope was initially analyzed in terms of the safety factor. The safety factor of the simple model was 1.13 at the undercut width of 150 m. The factor of safety was high enough for the working face of the mine, and coal mining in Area 4.1 was then deemed promising. After completion of the Area 4.1 mine plans and design, numerical analyses of both Class A and B predictions were performed to evaluate the stability of the undercut Area 4.1. The factors of safety of the 1st and 2nd Stages, based on the Class A and Class B predictions, respectively, were confirmed as 1.15 to 1.28 and 1.07, respectively.

During the mine development and mining of both Stages in Area 4.1, the monitoring system was employed to record all the geotechnical data related to slope stability, e.g., the precipitation, groundwater pressure, and surface and subsurface displacements. The surface and subsurface displacements from the monitoring data were compared with those from the numerical model. The displacements from the monitoring data and the numerical model were found to be comparable. In some regions, however, the displacements were unmatched both in magnitude and direction because of the complexity of the geology and the boundary conditions.

Conclusively, the coal exploitation in Area 4.1 was successfully completed without any serious accidents, injuries, or fatalities. The stability of the undercut Area 4.1 lasted for a year after the exploitation. This was a milestone brought about by the successful application of the numerical analysis to the design of a safe undercut face and the savings in mining costs of an open-pit mine. This novel undercutting method has the potential to increase the amount of mineable reserves and to make mining projects feasible and long-lasting. The undercutting technique is definitely an attractive and practical option for open-pit mine projects.

ACKNOWLEDGMENTS

REFERENCES

Boon, C. W., Houlsby, G. T., and Utili, S. (2014). "New insights into the 1963 Vajont slide using 2D and 3D distinct-element method analyses." *Geotechnique*, 64(10), 800-816.

Dawson, E. M., Roth, W. H., and Drescher, A. (1999). "Slope stability analysis by strength reduction." *Geotechnique*, 49(6), 835-840.

Eberhardt, E. (2012). "The Hoek–Brown Failure Criterion." *Rock Mech Rock Eng*, 45(6), 981-988.

EGAT (1985). *Thailand-Australia Lignite Mines Development Project,* Geotechnical Report, Mae Moh Mine.

EGAT (1990). *Interim Review of Geotechnical Strength Data*.

Gercek, H. (2007). "Poisson's ratio values for rocks." *International Journal of Rock Mechanics and Mining Sciences*, 44(1), 1-13.

Getzler, Z., Komornik, A., and Mazurik, A. (1968). "Model study on arching above buried structures." *Journal of the Soil Mechanics and Foundations Division - ASCE*, 94(SM5), 1123-1114.

Guo, P., and Zhou, S. (2013). "Arch in granular materials as a free surface problem." *Int. J. Numer. Anal. Methods Geomech.*, 37(9), 1048-1065.

Hoek, E. (2007). *Practical Rock Engineering*.

Hoek, E., and Bray, J. (1977). *Rock Slope Engineering*, The Institution of Mining and Metallurgy, London.

Hoek, E., Carranza-Torres, C., and Corkum, B. (2002). "Hoek-Brown Failure Criterion - 2002 Edition." *Proc., 5th North American Rock Mechanics Symposium*, 267-273.

Hoek, E., and Diederichs, M. S. (2006). "Empirical estimation of rock mass modulus." *International Journal of Rock Mechanics and Mining Sciences*, 43(2), 203-215.

Iglesia, G., Einstein, H., and Whitman, R. (2014). "Investigation of soil arching with centrifuge tests." *J. Geotech. Geoenviron. Eng.*, 140(2), 04013005.

Itasca Consulting Group, I. (2007). *3DEC: Theory and Background*, Minneapolis, MN.

Khosravi, M., Takemura, J., Pipatpongsa, T., and Amini, M. (2016). "In-flight excavation of slopes with potential failure planes." *J. Geotech. Geoenviron. Eng.*, 142(5), 06016001.

Khosravi, M. H., Pipatpongsa, T., Leelasukseree, C., and Wattanachai, P. (2009). "Failure mechanisms in arched excavation of sloped earth using model test." *Proc., Geo-Kanto 2009*, The Japanese Geotechnical Society, 241-246.

Khosravi, M. H., Pipatpongsa, T., Takahashi, A., and Takemura, J. (2011). "Arch action over an excavated pit in a stable scarp investigated by physical model tests." *Soils and Foundations*, 51(4), 723-735.

Khosravi, M. H., Pipatpongsa, T., Takemura, J., Mavong, N., and Doncommul, P. (2011). "Investigation on shear strength of shale at the Mae Moh open-pit mine." *Proc. of the 4th Thailand-Japan International Academic Conference (4th TJIA 2011)*, Thai Students' Association in Japan under the Royal Patronage, The University of Tokyo, 51-52.

Khosravi, M. H., Sarfaraz, H., Esmailvandi, M., and Pipatpongsa, T. (2017). "A Numerical Analysis on the Performance of Counterweight Balance on the Stability of Undercut Slopes." *International Journal of Mining and Geo-Engineering*, 51(1), 63-69.

Khosravi, M. H., Tang, L., Pipatpongsa, T., Takemura, J., and Doncommul, P. (2012). "Performance of counterweight balance on stability of undercut slope evaluated by physical modeling." *International Journal of Geotechnical Engineering*, 6(2), 193-205.

Leelasukseree, C., and Mavong, N. (2012). "Initial slope stability study of undercut slope at Area 4.1 Mae Moh mine, Lampang, Thailand." *21st Canadian Rock Mechanics Symposium 2012*, Canadian Institute of Mining, Metallurgy and Petroleum, 209-217.

Leelasukseree, C., Pipatpongsa, T., Khosravi, M. H., and Mavong, N. (2012). "Stresses and a failure mode from physical and numerical models of undercut slope lying on inclined bedding plane." *Proc., 7th Asian Rock Mechanics Symposium (ARMS2012)*, 1295-1304.

Matsui, T., and San, K.-C. (1992). "Finite element slope stability analysis by shear strength reduction technique." *Soils and Foundations*, 32(1), 59-70.

Mavong, N., Chaiwan, A., and Leelasukseree, C. "A rock mass elastic modulus estimation using Mae Moh mine's large scale experiment data." *Proc., ISRM European Regional Symposium - EUROCK 2014*, 241-245.

Mavong, N., Thepjun, A., and Leelasukseree, C. (2013). "Slope monitoring of large scale experiment of undercut slope at Mae Moh mine, Thailand." *Proc., 47th U.S. Rock Mechanics/Geomechanics Symposium*, American Rock Mechanics Association, 1237-1245.

Mungpayabal, N. (2005). *Residual shear strength of sheared Green Clay in Mae Moh mine*, Master of Engineeering Thesis, Chiang Mai University, Thailand.

Ohta, H., Pipatpongsa, T., Heng, S., Yokota, S., and Takemoto, M. (2010). "Significance of saturated clays seams for the stability of rainfall-induced landslides." *Bulletin of Engineering Geology and the Environment*, 69(1), 71-87.

Ono, K., and Yamada, M. (1993). "Analysis of the arching action in granular mass." *Geotechnique*, 43(1), 105-120.

Ouch, R., Ukritchon, B., and Pipatpongsa, T. (2016). "Stability of soil block on low interface friction plane with and without side supports." *Engineering Journal*, 20(2), 123-145.

Pipatpongsa, T., Khosravi, M. H., Doncommul, P., and Mavong, N. (2009). "Excavation problems in Mae Moh lignite open-pit mine of Thailand." *Proc., The Proceedings of Geo-Kanto2009*, The Japanese Geotechnical Society, 459-464.

Pipatpongsa, T., Khosravi, M. H., Leelasukseree, C., Mavong, N., and Takemura, J. (2010). "Slope failures along oblique plane due to sequential removals of propping portion in physical model tests." *The 15th National Convention on Civil Engineering, Engineering Institute of Thailand*, p.135 (CD-ROM).

Pipatpongsa, T., Khosravi, M. H., and Takemura, J. (2013). "Physical modeling of arch action in undercut slopes with actual engineering practice to Mae Moh open-pit mine of Thailand." *Proc., The 18th International Conference on Soil Mechanics and Geotechnical Engineering (ICSMGE18)*, 943-946.

Pipatpongsa, T., Khosravi, M. H., Takemura, J., Leelasukseree, C., and Doncommul, P. (2016). "Modelling concepts of passive arch action in undercut slopes." *Proc., The First Asia Pacific Slope Stability in Mining Conference*, Australian Centre for Geomechanics, 507-520.

Terzaghi, K. (1936). "Stress distribution in dry and in saturated sand above a yielding trap-door." *Proc., The First International Conference on Soil Mechanics and Foundation Engineering*, Harvard University, 307-311.

Ukritchon, B., Ouch, R., Pipatpongsa, T., and Khosravi, M. H. (2018). "Investigation of stability and failure mechanism of undercut slopes by three-dimensional finite element analysis." *KSCE Journal of Civil Engineering*, 22(5), 1730-1741.

INTERNATIONAL JOURNAL OF
GEOENGINEERING
CASE HISTORIES